iScience

Article

GPX4-dependent ferroptosis sensitivity is a fitness trade-off for cell enlargement

Graphical abstract

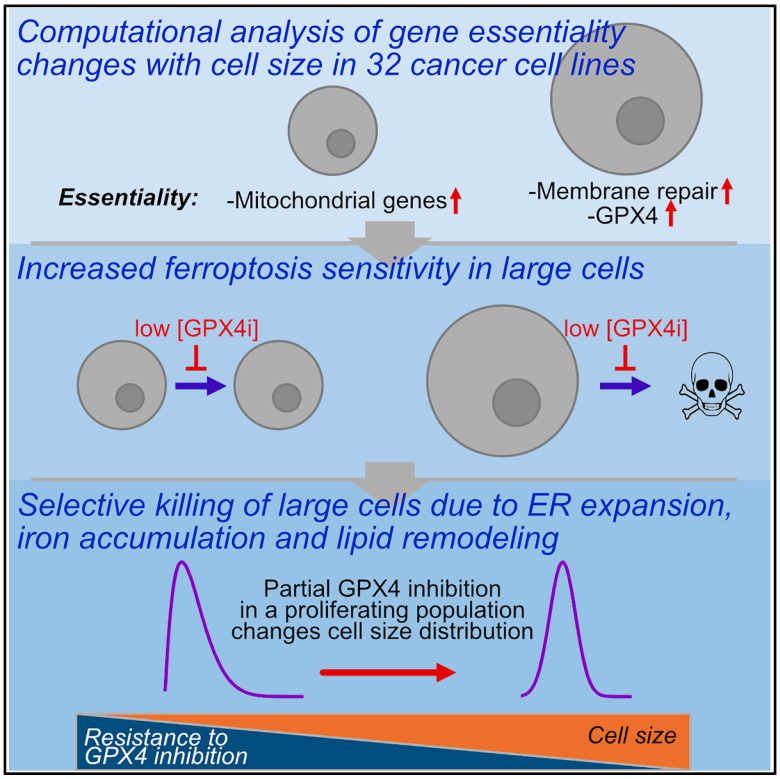

Highlights

- Cell size changes essentiality of mitochondrial, membrane repair, and ferroptosis genes
- Large cell size sensitizes cells to ferroptosis by GPX4 inhibition
- ER expansion, iron accumulation, and lipid remodeling contribute to a ferroptosis-sensitive cell state
- Lipid peroxidation may influence cell size homeostasis in proliferating cell populations

Authors

Kuan Yoow Chan, Yini Yu, Yidi Kong, ..., Junxia Min, Fudi Wang, Mikael Björklund

Correspondence

mikael.bjorklund.lab@gmail.com

In brief

Biochemistry; Molecular biology; Cell biology

Chan et al., 2025, iScience 28, 112363
May 16, 2025
https://doi.org/10.1016/j.isci.2025.112363

CellPress

iScience

CellPress
OPEN ACCESS

Article

GPX4-dependent ferroptosis sensitivity is a fitness trade-off for cell enlargement

Kuan Yoow Chan,[1,2] Yini Yu,[1] Yidi Kong,[1] Ling Cheng,[1] Renzhi Yao,[1] Phoebe Sha Yin Chair,[1] Ping Wang,[1] Rong Wang,[3] Wan-Yang Sun,[3] Rong-Rong He,[3] Junxia Min,[4] Fudi Wang,[5] and Mikael Björklund[1,2,6,*]

[1]Centre for Cellular Biology and Signalling, Zhejiang University-University of Edinburgh (ZJU-UoE) Institute, 718 East Haizhou Road, Haining 314400, China

[2]Edinburgh Medical School: Biomedical Sciences, College of Medicine and Veterinary Medicine, University of Edinburgh, Edinburgh EH8 9JZ, UK

[3]Guangdong Engineering Research Center of Traditional Chinese Medicine & Disease Susceptibility/Guangzhou Key Laboratory of Traditional Chinese Medicine & Disease Susceptibility/Guangdong-Hong Kong-Macao Universities Joint Laboratory for the Internationalization of Traditional Chinese Medicine/International Cooperative Laboratory of TCM Modernization and Innovative Drug Development of Chinese Ministry of Education (MOE)/Guangdong Province Key Laboratory of Pharmacodynamic Constituents of TCM and New Drugs Research/State Key Laboratory of Bioactive Molecules and Druggability Assessment, Jinan University, Guangzhou 510632, China

[4]The First Affiliated Hospital, Institute of Translational Medicine, Zhejiang University School of Medicine, Hangzhou 310058, China

[5]The Second Affiliated Hospital, School of Public Health, State Key Laboratory of Experimental Hematology, Zhejiang University School of Medicine, Hangzhou 310058, China

[6]Lead contact

*Correspondence: mikael.bjorklund.lab@gmail.com

https://doi.org/10.1016/j.isci.2025.112363

SUMMARY

Despite wide variation, each cell type has an optimal size. Maintaining optimal size is essential for cellular fitness and function but the biological basis for this remains elusive. Here, we performed fitness analysis involving genome-wide CRISPR-Cas9 knockout data from tens of human cell lines and identified that cell size influences the essentiality of genes related to mitochondria and membrane repair. These genes also included glutathione peroxidase 4 (GPX4), which safeguards membranes from oxidative damage and prevents ferroptosis—iron-dependent death. Growth beyond normal size, with or without cell-cycle arrest, increased lipid peroxidation, resulting in a ferroptosis-sensitive state. Proteomic analysis revealed cell-cycle-independent superscaling of endoplasmic reticulum, accumulation of iron, and lipidome remodeling. Even slight increases from normal cell size sensitized proliferating cells to ferroptosis as evidenced by deep-learning-based single-cell analysis. Thus, lipid peroxidation may be a fitness trade-off that constrains cell enlargement and contributes to the establishment of an optimal cell size.

INTRODUCTION

Cell size represents a fundamental trait across organisms from bacteria to eukaryotes. Increased cell size can offer evolutionary advantages. For example, in Lenski's long-term experiment over 50,000 generations, *Escherichia coli* cells grew larger and showed improved fitness across all evolving populations.[1,2] In eukaryotic evolution, the emergence of mitochondria, an essential bioenergetic organelle, coincided with cell size expansion.[3] Although these observations suggest that a cell size increase can be beneficial on an evolutionary timescale, enlarged cell size in mammalian cells is a hallmark of senescence,[4,5] and mitochondrial functionality declines with increased cell size in cultured cells and *in vivo*.[6–9] These observations indicate that certain physical limitations or biological factors antagonize the increase in cell size. This paradox raises intriguing questions about the evolutionary constraints that shape cell size and the mechanisms that reconcile the apparent conflict between long-term evolutionary benefits and short-term fitness trade-offs of increased cell size.

The potential drivers that cause cell size to gravitate toward the optimum size either during evolution[10] or to maintain cell size homeostasis[11] remain unknown. Identification of such drivers in mammalian cells would likely require experimental approaches that extend beyond one or two cell types as is commonly done. For cancer studies, Cancer Dependency Map (DepMap) CRISPR/Cas9 knockout (KO)-screen-based gene essentiality data are now available for hundreds of human cell lines,[12–14] allowing statistical associations with protein and gene expression levels to identify cancer vulnerabilities beyond single cell types. We reasoned that these data could also indicate which biological processes are limiting cell growth and cellular fitness across multiple cell lines. We therefore associated DepMap KO data with the average cell sizes of 32 human cancer cell lines[15] to identify common fitness trade-offs linked to cell size on a genome-wide scale.

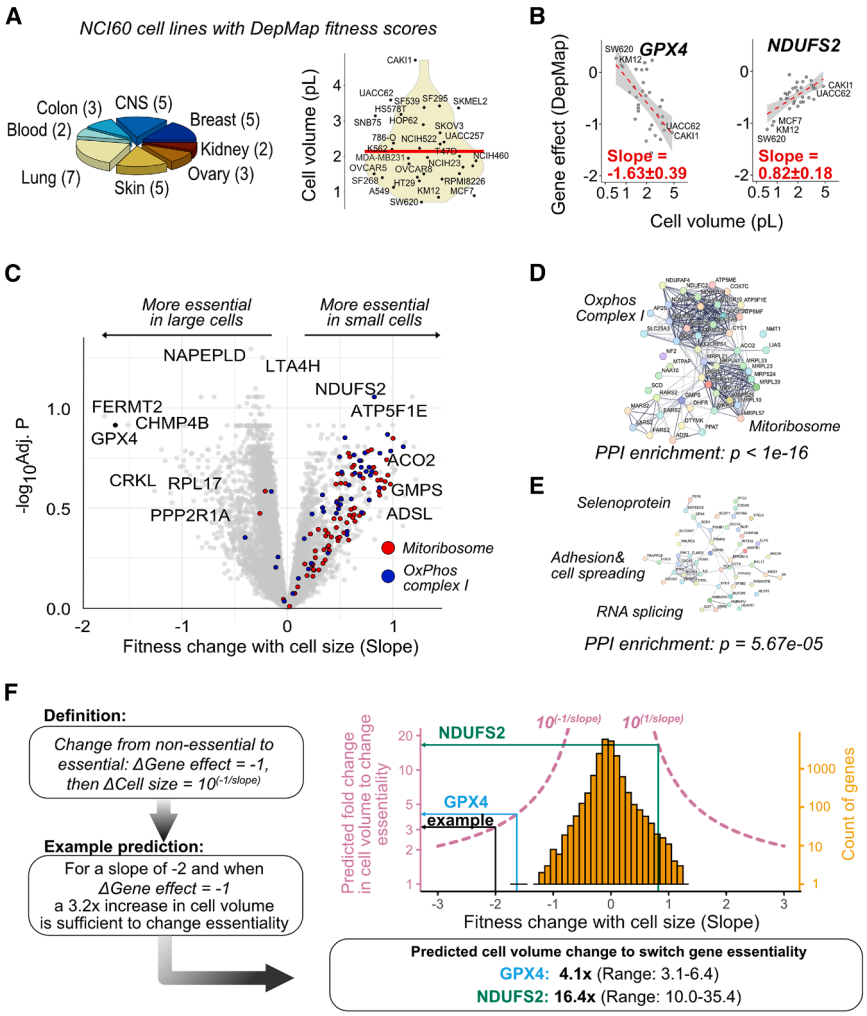

Figure 1. Gene essentiality profiling across 32 cell lines associates mitochondria, plasma membrane repair, and ferroptosis with cell size

(A) Outline for the computational cell size fitness analysis. (Left) Tissue distribution of the 32 cell lines with cell size data and fitness scores (gene essentiality). CNS, central nervous system. (Middle) Violin plot of the cell size distributions of the cell lines. The mean cell size is indicated with the horizontal red line. (Right) Schematic for correlation of cell size with DepMap gene effects.

(B) DepMap gene effect as a function of cell volume for GPX4 and NDUFS2. The linear model shows regression (red dotted line) and standard error (gray shaded area). Mean slope and standard error is indicated.

(C) Volcano plot depicting fitness changes with cell size (slope) as well as the statistical significance of the associations with cell size for all genes. Mitochondrial OxPhos complex I and mitochondrial ribosomal (mitoribosome) genes are indicated with blue and red, respectively.

(D) String network analysis of genes that are more essential in small cells and less essential in large cells. The *p* value for the protein-protein interaction enrichment is indicated below the network.

(E) String network analysis of genes that are more essential in large cells.

(F) Model depicting the relationship between cell size and slope to change a gene from non-essential to essential (Δgene effect = −1). The model prediction with slope −2 results in ~3-fold increase in cell size to switch gene essentiality. The histogram (right) shows distribution of the slopes, whereas the pink response curves mark the required cell volume change for each slope value. The predicted cell volume changes for GPX4 and NDUFS2 are indicated. See also Figure S1 and Data S1 and S2.

Here, we show that larger cell size associates with reduced essentiality of many mitochondrial and increased essentiality of plasma membrane repair genes. Glutathione peroxidase 4 (GPX4), the cellular guardian against membrane lipid peroxidation and a key regulator of iron-dependent cell death known as ferroptosis,[16] was identified as a top hit. Ferroptosis is an ancient vulnerability caused by oxidized polyunsaturated lipids in cellular membranes,[16] and it has been connected to many human diseases, including cancers, neurodegeneration, inflammation, and infections.[17] Our proteomics, lipidomics, imaging, and functional analyses indicate endoplasmic reticulum (ER) expansion with iron and lipid accumulation and lipidome remodeling. These changes make large cells susceptible to lipid peroxidation and ferroptosis when GPX4 is inhibited or absent. Our results highlight the importance of optimal cell size for cellular health, provide a compelling reason why cells need to control their size, and inform a rational strategy for eliminating large senescent cells in aging tissues and certain cancers using GPX4 inhibitors.

RESULTS

Essentiality of genes related to mitochondria and membrane repair changes with cell size

We identified a subset of 32 cell lines from the NCI60 cancer cell line panel for which both gene essentiality scores and the mean cell size of the populations are available[15] (Figure 1A, Data S1). The cell sizes covered by NCI60 cell lines span a range that covers a large fraction of sizes observed in different human cell types,[18] although excludes adipocytes, myocytes, and neurons on the largest end and blood cells on the smallest end (Figure S1A). We statistically associated cell sizes and gene essentiality scores using linear modeling as done previously for molecular markers.[12,14,19] Two example genes, GPX4, a gene suppressing lipid peroxidation and ferroptosis, and mitochondrial electron transport chain complex I subunit NDUFS2, which is known to be essential for complex I activity,[20] displayed clear and opposite trends of cell-size-dependent gene essentiality in the 32 cell lines analyzed (Figure 1B). Visualization of the

complete data for all genes further revealed that mitochondrial oxidative phosphorylation (OxPhos) complex 1 subunits and mitochondrial ribosomal protein genes were enriched for reduced essentiality in larger cells (Figures 1C and 1D). This is consistent with the previously identified reduction of mitochondrial functionality in large cells both in culture and *in vivo*,[7,9] thus validating our approach. Genes enriched for increased essentiality (reflecting reduced fitness) in larger cells were related to RNA splicing, selenoproteins, adhesion, and cell spreading (Figure 1E). The strongest hits with increased essentiality in larger cells included GPX4, CHMP4B, a component of the ESCRT-III complex required for membrane repair,[21] and FERMT2, a protein required for plasma membrane integrity.[22] Other strong hits included focal adhesion regulators CRKL, CDC42, RAC1, CDC42, PTK2/FAK1, and a little studied phagocytic gene NHLRC2.[23]

Permutation-based control analyses were performed by randomly associating the cell size values with the essentiality data in the same set of cell lines. This analysis ranked the t statistics of GPX4 in the actual screen as the top scoring one among 10,000 permutations. Similarly, OxPhos complex I subunits as an aggregate were ranked 9th among 1,000 permutations (Figure S1B). Enrichment of mitochondrial essentiality was identified using both the magnitude of the fitness change (slope) or the statistical significance (t statistics for the linear model) (Figure S1C), indicating large and consistent fitness effects across tens of different cancer cell lines. In addition to gene essentiality scores, the DepMap project also includes additional data. As done with the gene essentiality scores, we similarly associated cell size with gene copy numbers in all the 57 of the NCI60 cell lines for which the copy-number data were available (Figure S1D, Data S2). This analysis also enriched mitochondrial genes as well as GPX4 and genes related to arachidonic acid metabolism, a major substrate for lipid peroxidation.[24] Furthermore, among the 38 of the NCI60 cell lines for which drug sensitivity data were available, top associations with cell size included Trolox and TEMPOL, two reactive oxygen species scavengers that can inhibit ferroptosis, suggesting that lipid peroxidation and ferroptosis sensitivity associate with cell size regardless of the specific dataset (Figure S1D, Data S2). Altogether, these statistical associations across tens of different proliferating human cell lines suggest that large cell size is associated with lipid peroxidation and ferroptosis.

The identified associations do not directly tell us whether the top changes in gene essentiality are sufficiently large to be physiologically relevant and if they can occur during cell enlargement of individual cells within a cell population. We therefore first asked if the change in essentiality of any of the genes would be able to alter cellular fitness within an achievable range of cell sizes. The linear regression model based on the data from the 32 cell lines can be applied to predict the necessary change in cell size for a one-unit shift in gene essentiality score, which by DepMap data definition separates known essential genes from the non-essential ones (Figure 1F). Therefore, a one-unit shift represents the transition of a gene from being non-essential to essential (or vice versa). For example, for a steep slope of the linear model, a smaller change in cell size will result in the one-unit shift in the gene essentiality score, whereas for a shallow slope, a much larger cell size change is required for the one-unit shift in gene essentiality score. Since the slope of our regression analysis represents the rate of change in gene essentiality score per unit change in the logarithm of cell size, the required cell size change to switch essentiality can be calculated as ΔCell size = $10^{(-1/\text{slope})}$. Consequently, the response curve depicted in the Figure 1F is nonlinear when viewed in terms of the original, untransformed cell size values. For example, a slope of -2 requires a 3.2x increase in cell volume to change essentiality of a gene (see the example in Figure 1F). We can then calculate from the slopes of the linear models of individual gene data that for GPX4 and NDUFS2, a 4.1x and a 16.4x change in cell volume is required, respectively. To estimate the error of these predictions, we use the standard error of the slope, which results in a volume change estimate of 3.1–6.4 for GPX4 and 10.0–35.4 for NDUFS2. Therefore, a complete switch of gene essentiality in cell culture is likely confined to a few top scoring genes because it requires relatively large cell size changes. However, a smaller change in cell size might be sufficient for an increased (or decreased) sensitization to the loss of the top genes.

Large cell size, not a cell-cycle arrest, sensitizes cells to ferroptosis via GPX4 inhibition

To experimentally validate that gene essentiality can be altered by cell size, we inhibited GPX4 activity in retinal pigment epithelium (RPE1) cells, an immortalized normal diploid cell line that was not part of our analysis of the DepMap data. Thus, RPE1 cells serve as an independent, non-cancerous model to validate the computational analysis. Two drugs, DNA damage inducer doxorubicin and cyclin-dependent kinase (CDK) 4/6 inhibitor palbociclib, are commonly used to increase cell size. When RPE1 cells were treated for 3 days with these drugs, the cells became approximately 3-fold larger during the cell-cycle arrest induced by these drugs (Figure 2A). These enlarged RPE1 treated with a GPX4 inhibitor RSL3 displayed increased sensitivity to cell death compared to normal-sized proliferating cells (Figure 2A, right). Cells treated with a combination of RSL3 and Fer-1, a well-established ferroptosis inhibitor, were resistant to cell death, indicating specificity. To quantify the sensitization to ferroptotic cell death, we titrated RSL3 and measured cell viability using the CellTiter-Glo assay. The effective concentration (EC_{50}) of RSL3 displayed a $\sim$3,000x difference between normal-sized and large cells (Figure 2B). However, such a huge difference was not observed with all batches of fetal bovine serum, which varies in antioxidant capacity and lipid content. More commonly a 100–300x increase in RLS3 sensitivity was observed in RPE1 cells. Other GPX4 inhibitors (e.g., ML162 and FIN56) also displayed more than a 100x increase in sensitivity in large cells (Figures S1F–S1H). In contrast, cell size did not influence sensitivity to erastin or sulfasalazine, which induce ferroptosis through the plasma membrane cystine-glutamate antiporter system x_C^- (Figures 2B, S2A, and S2B). Because thioredoxin reductase (TXNRD1) is potentially an off-target for RSL3 and ML162,[25] we also tested TXNRD1 inhibitors auranofin and TRi-1. These compounds did not display cell size dependency (Figure S2B). Overall, these data indicate that on-target GPX4 inhibition is responsible for the death of large cells. This

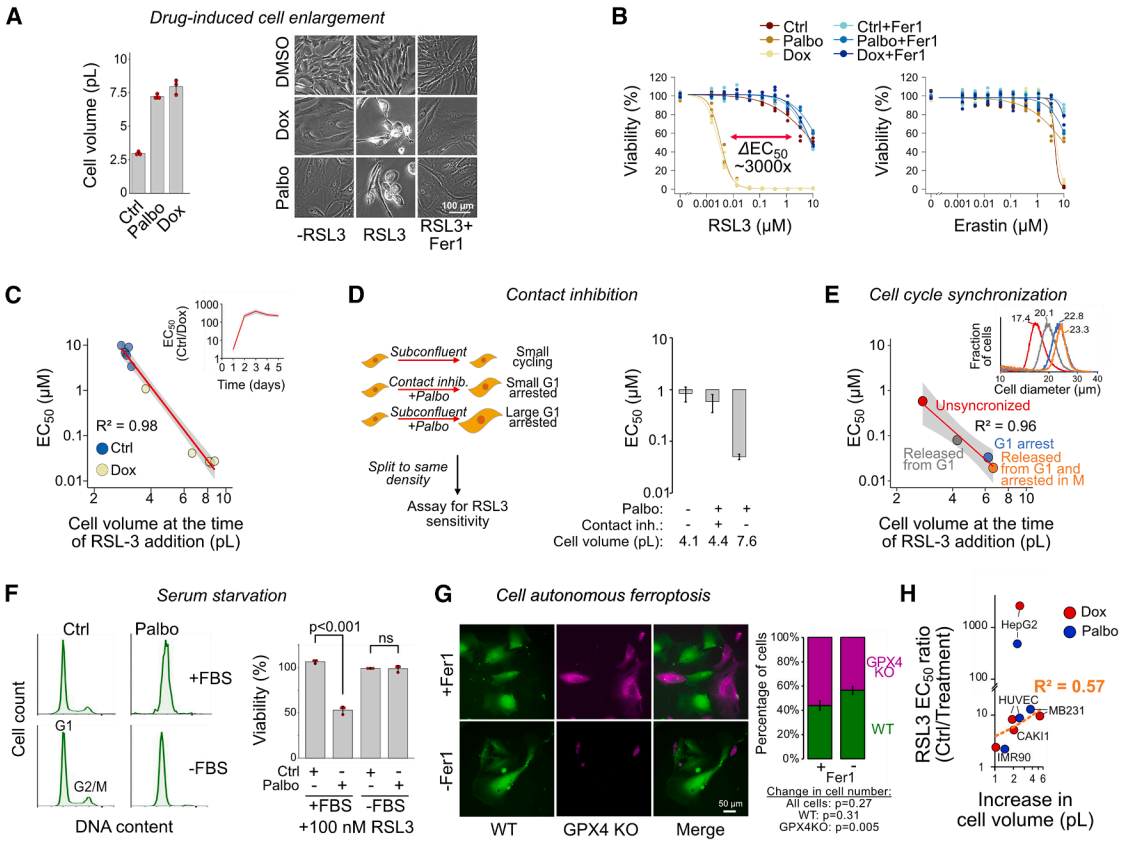

Figure 2. Increased ferroptosis sensitivity in large cells is not due to a cell-cycle arrest

(A) Cell diameters measured with Coulter Counter for RPE1 control cells and cells treated with 1 μM palbociclib and 50 nM doxorubicin for 3 days and photomicrographs showing their sensitivity to 1 μM RSL3 with and without 1 μM ferrostatin-1 (Fer-1). Data shown are mean ± SD, *n* = 3, with individual replicate values in red.

(B) Quantification RSL3 (left) and erastin sensitivity (right) of control, palbociclib-treated, and doxorubicin-treated RPE1 cells with and without 1 μM Fer-1. The change in ferroptosis sensitivity of the larger palbociclib- and doxorubicin-treated cells compared to control cells is indicated (ΔEC_{50}). The kill curve is fitted based on three replicates for each ferroptosis inducer concentration, and each experiment was repeated minimum two times.

(C) Correlation between cell volume at the time of RSL3 addition and RSL3 sensitivity (EC_{50}) using a time course of control and doxorubicin-treated cells. Linear model (red line) with standard error (gray). The inset shows time-dependent increase in ferroptosis sensitivity.

(D) Ferroptosis sensitivity in G1-arrested cells when palbociclib-induced cell size increase is limited via contact inhibition. Bar chart shows mean and standard deviation of ferroptosis sensitivity from triplicate samples.

(E) Correlation between cell volume at the time of RSL3 addition with RSL3 sensitivity (EC_{50}) from cell-cycle-synchronized, arrested, and releasing RPE1 cells in different phases of the cell cycle. STLC: kinesin inhibitor S-trityl-l-cysteine (STLC). Cell size distributions and the mean diameter of each population are indicated in top right.

(F) DNA content by flow cytometry for control and palbociclib-treated cells in the presence or absence of FBS. (Right) Viability of the same cells treated with 0.1 μM RSL3 for 24 h. Data shown are mean ± SD, *n* = 3 normalized to cells without RSL3. Statistical significance by ANOVA followed by Tukey's post-hoc test.

(G) Co-culture of RPE1 WT and GPX4 KO cells arrested with X-rays and grown for 3 days before removing ferroptosis inhibitor Fer-1. (Right) Quantification of the percentage of cell with and without Fer-1. Quantification is mean ± SEM, with statistical testing from cell counts from 12 fields with two-sided t test.

(H) The relative sensitization to RSL3 as a function of cell size increase compared to DMSO control cells in different cell lines. HepG2 samples were excluded as outliers from the linear regression. See also Figure.

is consistent with our computational fitness analysis, which did not associate cell size with system x_C^- genes (Data S1; Figure S2A), possibly because there are additional mechanisms to maintain glutathione levels to keep GPX4 functional, such as synthesis and regeneration of glutathione as well as reducing its consumption by other processes. As TXNRD1 contributes to ferroptosis by converting intracellular cystine to cysteine,[26] we further exclude a role for system x_C^- in cell-size-dependent ferroptosis sensitivity.

A 5-day time course experiment with control and doxorubicin-treated cells demonstrated a strong correlation between EC_{50} of RSL3 and cell volume at the time of cell death induction (R^2 = 0.98, Figure 2C). Since cell size is closely related to other growth-related parameters, we repeated the computational fitness analysis using ploidy, doubling time, cellular dry mass, and growth rate as the dependent variables (Data S1). The essentiality of GPX4, NDUFS2 as an example of a mitochondrial protein, and more generally mitochondrial translation and

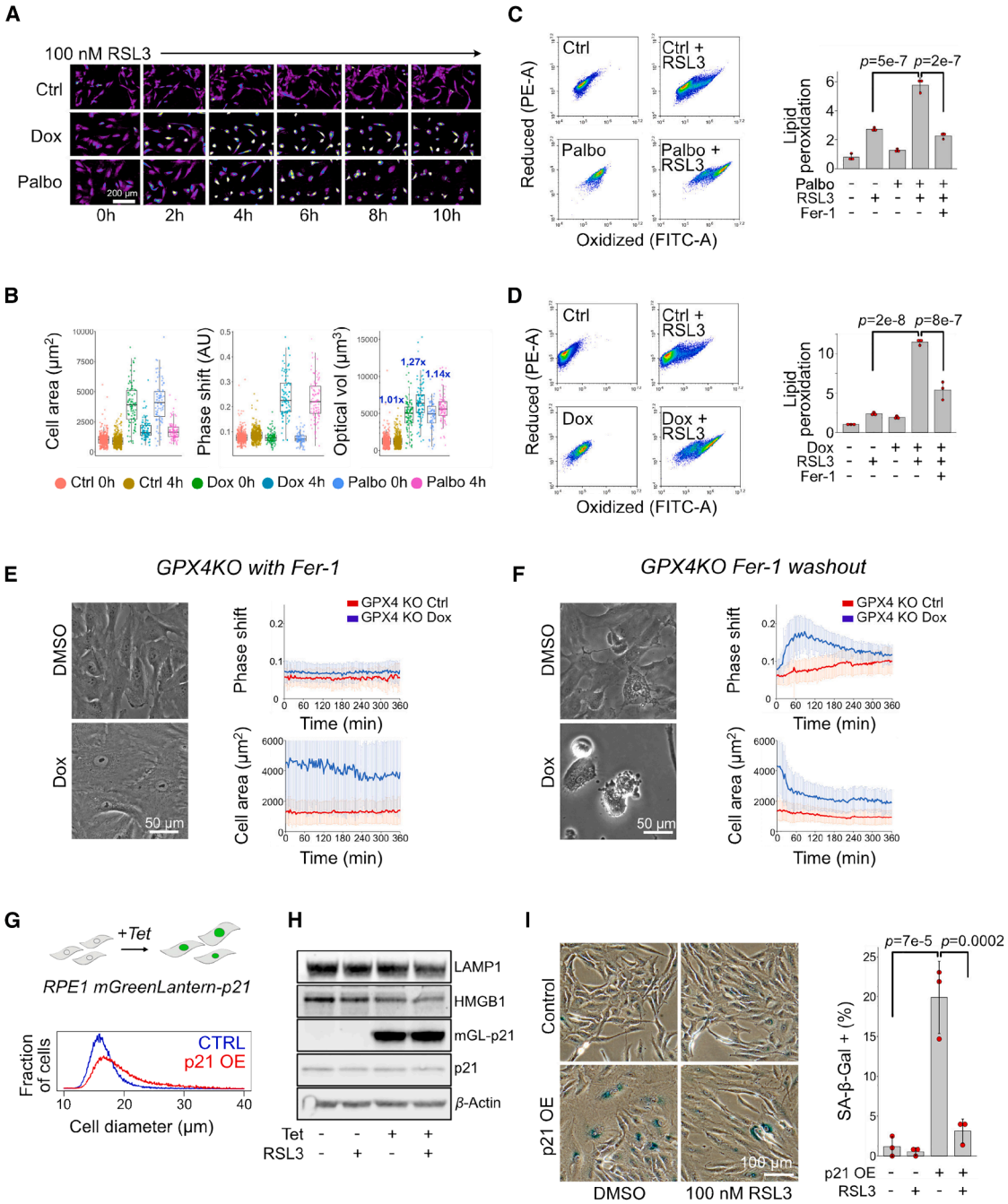

Figure 3. Increased lipid peroxidation in large cells

(A) Digital holography images of RSL3 treatment time course for control, doxorubicin-treated, and palbociclib-treated RPE1 cells.

(B) Quantification of imaging parameters at 0 and 4 h after RSL3 addition. The blue numbers in the optical volume indicate the increase in cell volume (swelling) between 0- and 4-h time points.

(C) Lipid peroxidation in RPE1 cells using C11-bodipy lipid peroxidation sensor and flow cytometry. Probe oxidation results in a shift of the fluorescence emission peak from red (PE-A) to green (FITC-A) channel. Cells treated with palbociclib were treated with or without 1 µM RSL3 and 1 µM Fer-1 as indicated. Data shown are mean ± SD, $n = 3$.

(D and E) (D) Same as (C) but cells were treated with 50 nM doxorubicin. Statistical analysis in (C and D) was ANOVA followed by Tukey's test. (E) Digital holographic quantification of cell areas and phase shifts for single GPX4 KO cells treated with (blue line) or without (red line) doxorubicin for 3 days after which they were imaged for 6 h in the presence of ferroptosis inhibitor Fer-1.

(F) Same treatment as in (E), but Fer-1 was washed out immediately before imaging. Mean values are in solid line, with error bars showing standard deviation; between 52 and 660 cells were tracked.

(legend continued on next page)

OxPhos had the strongest association with cell volume (Figure S2C). To exclude the possibility that increased sensitivity to ferroptosis was a consequence of a cell-cycle arrest[27] or a secondary effect of the drugs used, we treated RPE1 cells with palbociclib but varied the original cell seeding density to reduce cell growth by contact inhibition followed by re-seeding to similar cell density (Figure 2D). This approach yielded two cell populations, both arrested in G1 phase and treated with the same concentration of palbociclib for an equivalent duration. Of these two populations with average volumes of 4.4 and 7.6 pL, the larger cells had greater ferroptosis sensitivity (Figure 2D).

We next evaluated the effect of cell-cycle stage on ferroptosis sensitivity using unsynchronized cells, palbociclib-treated G1-arrested cells, as well as cells treated with palbociclib but released back to cell cycle or subsequently arrested in mitosis by the Eg5 kinesin inhibitor S-Trityl-l-cysteine (STLC) (Figure S2D). This resulted in four populations varying in cell-cycle stage, proliferative status, synchrony, and DNA content (Figure S2E). A high correlation between RSL3 sensitivity and cell size was again observed ($R^2 = 0.96$). To further show that ferroptosis sensitization is not simply due to a G1 arrest, we treated cells with palbociclib for 24 h. The G1-arrested cells were then cultured with palbociclib for another 48 h in the presence or absence of fetal bovine serum (FBS; serum starvation), to remove mitogens and growth factors that stimulate cell growth. Although both treatments maintained their arrested state, only the cells cultured in the presence of FBS showed reduced viability when treated with 100 nM RSL3 (Figure 2F). Thus, together with the contact inhibition experiments (Figure 2D), these data indicate that cell overgrowth and not the exposure to palbociclib alone is required for increased ferroptosis sensitivity. Additional control experiments with knockout cells for G1 regulators RB1 and p21 indicated that these proteins are not directly related to cell-size-dependent ferroptosis sensitivity (Figures S2F and S2G).

To further rule out secondary effects of the drugs used and to test if the ferroptosis sensitization by cell size is cell autonomous, we labeled WT RPE1 and RPE1 GPX4 KO cells (Figure S2H) with distinct fluorescent tracker dyes. We mixed the stained cells for a co-culture and treated them with or without X-rays, which induced large cell size and increased ferroptosis sensitivity (Figure S2I). Removal of Fer-1 from the medium resulted in selective elimination of GPX4 KO cells, (Figure 2G) consistent with previous findings that ferroptosis induced by GPX4 inhibition is cell autonomous and does not propagate from cell to cell.[28]

As already suggested by the original computational analysis involving more than 30 cell lines, additional experiments demonstrated that the increased sensitivity to ferroptosis is not limited to RPE1 cells. Both normal (e.g., IMR-90, HUVEC) and cancer cell lines (e.g., HepG2, MDA-MB-231, CAKI-1) treated with either doxorubicin or palbociclib increased RLS3 sensitivity up to 1,000-fold. The relative increase in cell size (note the log scale for x axis) is linearly dependent on the relative increase in ferroptosis sensitivity (Figure 2H).

Overall, important conclusions can be drawn from these experiments. Although we associate the absolute cell size in the NCI60 cell panel with the ferroptosis sensitivity, we note that as the baseline ferroptosis sensitivity of the cell lines varies substantially, it may not particularly be informative to compare absolute sizes of different cell lines. Furthermore, ferroptosis sensitivity changes with cell size and not due to a cell-cycle arrest. Finally, because GPX4 is intracellular and system x_C^- is plasma membrane localized, surface-to-volume ratio, a common explanation for cell size effects, is not a determinant of ferroptosis sensitivity.

Lipid peroxidation increases with cell size independently of GPX4

Digital holography, a label-free quantitative phase imaging technique, revealed that ferroptotic cell death in large cells occurred rapidly upon GPX4 inhibition. After 4 h of RSL3 addition, most large cells displayed decreased cell area as well as an increased average phase shift, indicative of changes in cellular thickness and refractive index, respectively. These measurements are consistent with rounding up of dying cells (Figures 3A and 3B). Cells undergoing ferroptotic death are also characterized by swelling.[28,29] Quantification of swelling by optical volume measurement demonstrated a 15%–25% increase in large cells treated with RSL3 (Figure 3B).

We next used Bodipy-C11 lipid peroxidation sensor with flow cytometry and observed increased lipid peroxidation in both palbociclib- and doxorubicin-treated large cells (Figures 3C and 3D). Lipid peroxidation correlated with cell size (Figures S3A and S3B). Fluorescent microscopy confirmed the increased oxidized Bodipy-C11 signal in RSL3-treated large cells (Figure S3C). Cell death induced by RSL3 treatment in doxorubicin-treated cells was prevented by Fer-1, antioxidants α-tocopherol (vitamin E), mitoquinone, and mitoquinol, iron chelator desferrioxamine mesylate, as well as by necrostatin-1, which is a radical trapping antioxidant and potent ferroptosis inhibitor. In contrast, apoptosis inhibitor Z-VAD-FMK was inactive (Figure S3D). Cell death inhibition by antioxidants and other known ferroptosis inhibitors supports the idea that increased lipid peroxidation in large cells is a driving factor for the observed ferroptosis sensitivity.

A minor reduction was observed in GPX4 levels by western blotting while expression of two other anti-ferroptosis proteins, DHODH and FSP1, also displayed slightly reduced expression (Figure S3E). To test if ferroptosis sensitization was due to changes in GPX4 expression and/or activity, we used GPX4 KO cells. Phase shift and cell area in cells treated with and without doxorubicin remained stable in the presence of Fer-1 (Figure 3E). Upon removal of Fer-1, the larger doxorubicin-treated GPX4 KO cells rounded up within 1 h (Figure 3F). In contrast, control cells displayed a slower change of area and phase shift throughout the whole 6-h observation period.

(G) Tetracycline-inducible expression of mGreenLantern-p21. The cell size distribution with and without Tet-induction for 3 days was measured with coulter counter.

(H) WB analysis of mGreenLantern-p21 with and without Tet-induction for 3 days, followed by 100 nM RSL3 for 24 h. (I) Senescence-associated β-galactosidase staining of mGreenLantern-p21 cells. Data shown are mean ± SD, $n = 3$. ANOVA with Tukey's test. See also Figure S3.

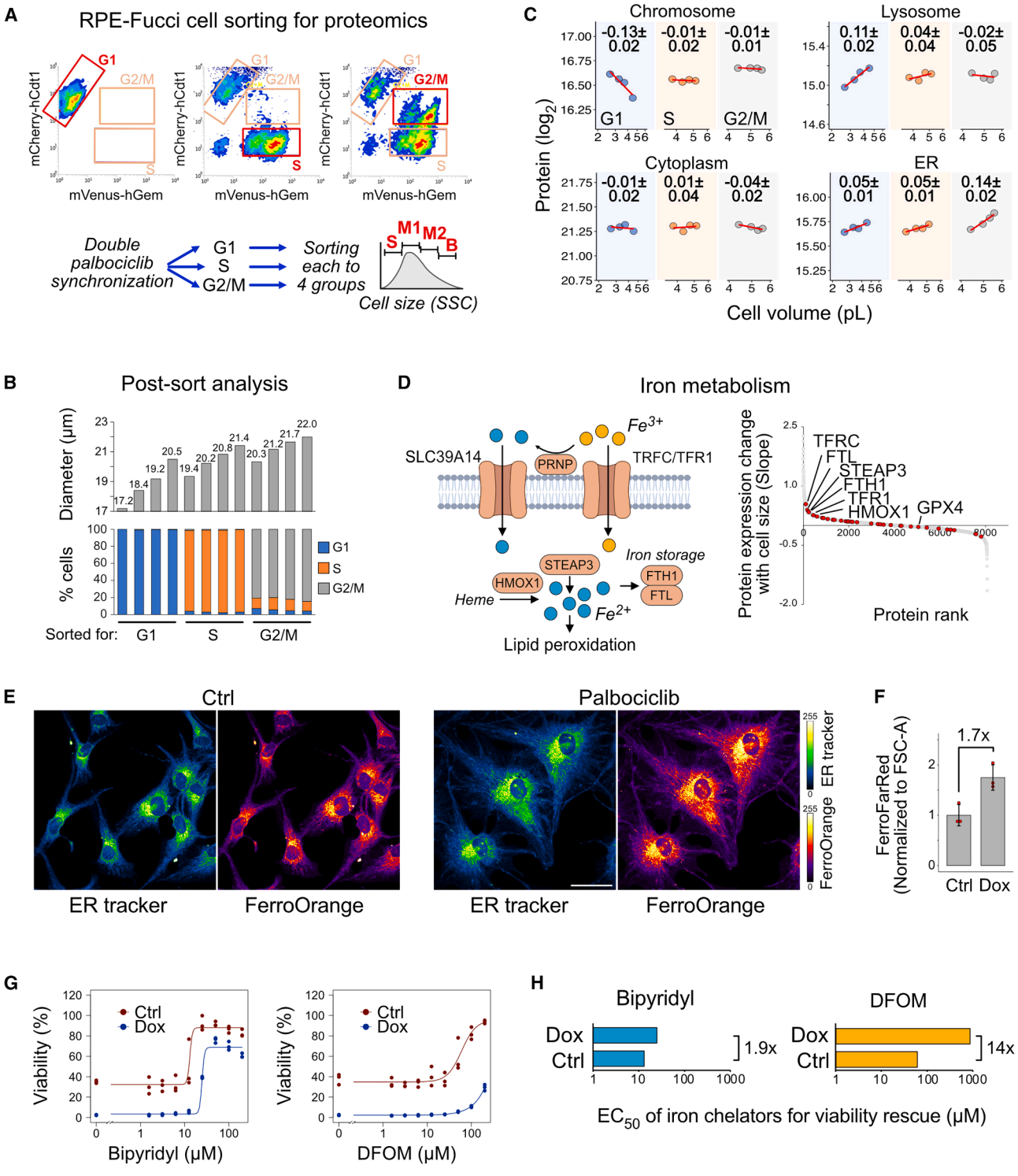

Figure 4. ER superscaling and iron accumulation are cell-cycle-independent ferroptosis sensitizers in large cells

(A) Strategy for sorting palbociclib-synchronized cells by cell cycle and cell size.

(B) Average cell diameters (upper) and cell size distribution (lower) of the sorted fractions.

(C) Average protein expression of proteins annotated to specific subcellular localizations in each cell-cycle phase. The slope±SE for the regression line is indicated.

(legend continued on next page)

These data indicated that larger cells have increased lipid peroxidation that sensitizes cells to loss of GPX4 activity (see Figures 2H and S3F). Since senescent cells are characterized by large cell size[4] and ferroptosis induction by GPX4 inhibition is cell autonomous,[28] we tested if GPX4 inhibition could be potentially used to target senescent cells. To this end, we generated RPE1 cells expressing a tetracycline-inducible mGreenLantern-p21 as a model for cell-cycle-arrest-induced senescence (Figures 3G and S3G). Overexpression of p21 resulted in a broad range of cell sizes, providing an attractive model system for targeting large cells. GPX4 inhibition with 100 nM RSL3 modestly impacted senescence-related markers at the population level including expression of endogenous p21, stress and damage marker HMGB1, and lysosomal marker LAMP1 (Figure 3H), highlighting the challenge with the analysis of individual senescence markers in population level assays.[30] The effect of RSL3 was more clear with senescence-associated β-galactosidase staining (Figure 3I).

Proteomic analysis identifies ER expansion and iron accumulation that are dependent on cell size but independent of the cell cycle

We next took a proteomics approach to identify the cellular processes that could explain the increased ferroptosis sensitivity. We synchronized RPE1-FUCCI (fluorescent ubiquitination-based cell cycle indicator) cell-cycle reporter line using a transient double palbociclib block, which resulted in a well-synchronized G1 arrest without excessive increase in cell size. We either directly sorted the resulting G1 cells by cell size using flow cytometry or released the cells for 8 and 12 h to sort cells by size in S and G2/M phases, respectively (Figure 4A). From each of these cell-cycle phases, we collected four fractions by cell size based on side scatter (SSC), which we found to best reflect cell size with the cytometer used. The mean diameters and cell-cycle distributions of the resulting 12 fractions were confirmed post-sorting (Figure 4B). In total, we detected 8,072 individual proteins in all the fractions (Data S3). The average expression of proteins known to localize to different subcellular compartments displayed the expected cell-size-dependent reduction in chromosomal and increase in lysosomal proteomes,[31] whereas cytoplasmic proteins remained constant (Figure 4C). However, these cell-size dependent changes in chromosomal and lysosomal proteomes were G1 phase specific. In contrast, cell-size dependent increase in ER proteome occurred in all phases of the cell cycle (Figure 4C).

ER has been indicated as the main site for lipid peroxidation in ferroptosis.[24,32] We confirmed ER expansion in large palbociclib-treated cells by western blot of well-known ER proteins (Figure S4A). Perturbation of ER expansion by inhibiting IRE1 endonuclease[33] by the small molecule STF-083010 reduced ER protein levels and cell size. ER expansion in large cells was further confirmed by RNA sequencing (RNA-seq) in doxorubicin-treated RPE1 cells as well as microcopy in cells treated with palbociclib (Figures S4B–S4D, Data S4). Varying concentrations of STF-083010 followed by flow cytometry analysis or ER-tracker-stained cells showed that ER content increased more than proportionally to the cell size (slope = 1.5 ± 0.1, Figure S4E). Reduction of ER expansion by STF-083010 reduced ferroptosis sensitivity, whereas a high correlation between cell size and ferroptosis sensitivity was maintained (Figures S4F and S4G). Knockout of IRE1 similarly reduced ferroptosis sensitivity (Figure S4H).

Proteomics analysis further indicated that iron-metabolism-related proteins such as ferritin light chain (FTL) and ferrireductase STEAP3, which reduces Fe^{3+} to Fe^{2+}, increased with cell size in each cell-cycle phase (Figures 4D and S4I). Indeed, when the proteome was sorted by the magnitude of expression change as the function of cell size (slopes of the linear model), iron-metabolism-related ferroptosis genes showed the largest changes in protein expression among the known ferroptosis genes (Figure 4D). This was confirmed by RNA-seq analysis (Figure S4J). These observations are consistent with the observations that genes related to iron metabolism increase in ferroptosis.[17] FerroOrange, a dye that labels labile intracellular divalent iron (Fe^{2+}), co-localized with ER tracker, confirming the reported ER localization of FerroOrange (Figure 4E). However, it is not known if the targeting to ER is due to highest intracellular iron levels in this organelle or because of the molecular characteristics of this dye. FerroOrange intensity was higher in palbociclib-treated large cells indicative of an increase in iron content. We quantified iron content by flow cytometry of a second iron-specific dye, FerroFarRed. This analysis showed a 1.7-fold increase in iron when normalized to cell size (~5-fold increase per cell) (Figure 4F). We then analyzed if the increased iron content contributes to lipid peroxidation. RSL3 was added to control and doxorubicin-treated cells in the presence of varying concentrations of two iron chelators, desferoxamine mesylate (DFOM) and bipyridyl. Depending on the iron chelator, 2–14 times higher concentrations were required to rescue ferroptosis sensitivity in large cells (Figures 4G and 4H), suggesting that increased iron content contributes to increased lipid peroxidation in large cells.

Lipid accumulation and remodeling in large cells

In addition to iron, cellular lipid content and composition are key factors in ferroptosis sensitivity.[34] Previous analyses have demonstrated that large cells have more lipids.[35] Consistently, doxorubicin-treated RPE1 cells had a higher lipid content as measured by a triglyceride assay (Figure 5A) and mass

(D) Effect of cell size on iron metabolism. Schematic of proteins involved in iron metabolism (left) and proteins ranked by the change of their levels as a function of cell size (right). Ferroptosis proteins are indicated with red dots.
(E) Maximum projection false-color images of ER tracker and FerroOrange fluorescence in control (left) and palbociclib-treated (right) cells. Scale bar: 50 μm.
(F) Flow cytometric quantification of iron content in control and doxorubicin-treated cells using FerroFarRed dye. Data shown are normalized to cell size (FSC-A) with the fold change indicated. Mean ± SD, $n = 3$.
(G) Change in ferroptosis sensitivity in control and doxorubicin-treated cells by iron chelators bipyridyl and desferoxamine (DFOM). Ferroptosis was induced with 1 μM RSL3 in the presence of varying concentrations of the iron chelators.
(H) Bar chart displaying the change in EC_{50} from data in (G). See also Figure S4 and Data S3 and S4.

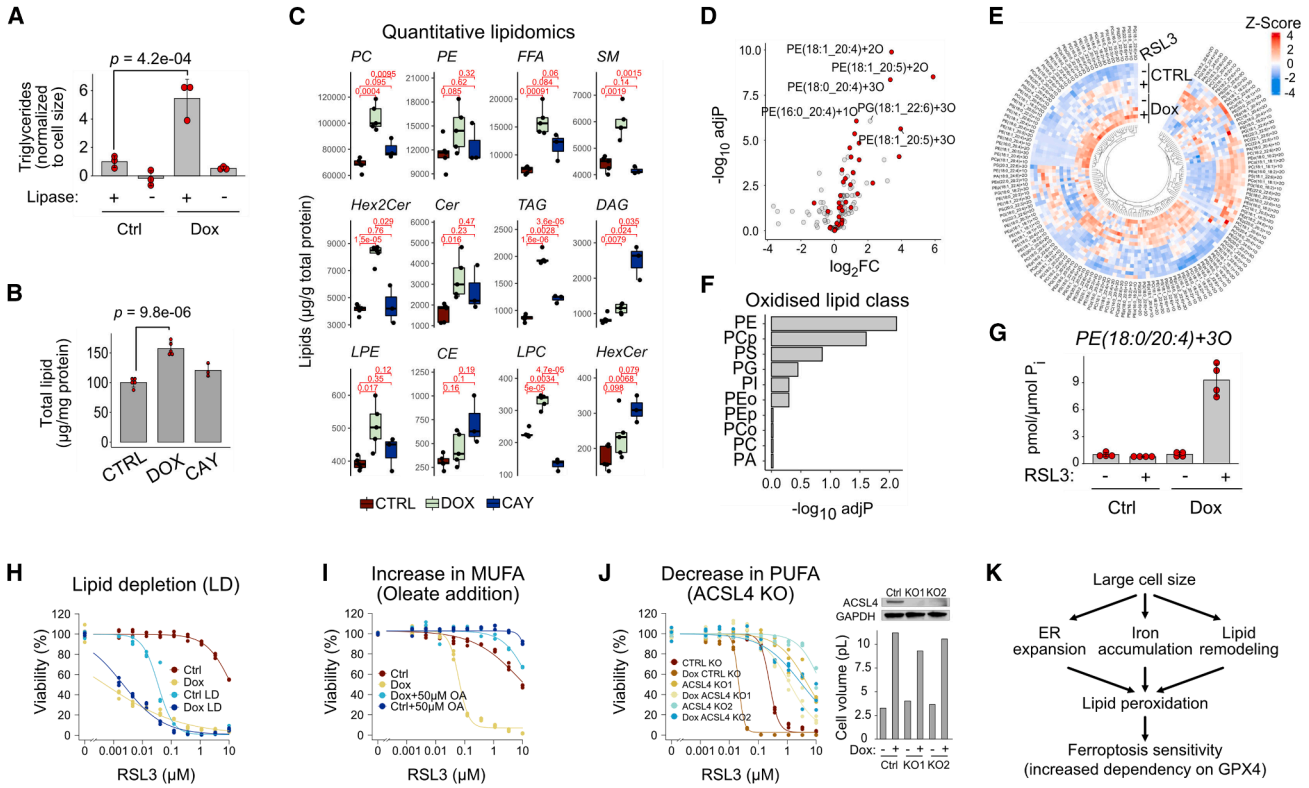

Figure 5. Lipid accumulation and remodeling in large cells

(A) Triglyceride levels normalized to cell size in control and doxorubicin-treated cells. No lipase controls show assay background originating from free glycerol. Data shown are mean ± SD, *n* = 3.

(B) Total lipids in control, doxorubicin, and desaturase inhibitor CAY10566 (CAY) by quantitative lipidomic analysis by mass spectrometry. Total lipid signals were integrated and normalized to protein concentration. Data shown are mean ± SD, *n* = 5, except for CAY for which only three replicates were used.

(C) Quantification of different lipid classes. Statistical significance by ANOVA followed by Tukey's post-hoc test.

(D) Volcano plot showing log2 fold changes and significance of the changes in oxidized lipids between doxorubicin-treated and control cells after RSL3 addition. Phosphatidylethanolamines (PEs) are in red.

(E) Heatmap of the redox lipidomic data (see Data S6 for details).

(F) Enrichment of oxidized lipids in different lipid classes. The subscripts o and p refer to oxidized and phosphorylated lipid, respectively.

(G) Quantification of a ferroptotic lipid marker PE(18:0/20:4)+3O. Data shown are mean ± SD, *n* = 4.

(H) Ferroptosis sensitivity of control and doxorubicin-treated RPE1 cells in the presence of normal or lipid depleted serum (LD).

(I) Ferroptosis sensitivity of control and doxorubicin-treated RPE1 cells with exogenous addition of 50 µM oleate (OA).

(J) Sensitivity of control KO cells and two clones of ACSL4 KO cells (KO1 and KO2) to RSL3 with and without doxorubicin treatment. Inset shows western blot with ACSL4 antibody and measured cell sizes.

(K) Model of ferroptosis sensitization involving ER expansion (Figure 3), iron accumulation (Figure 4), and lipidome remodeling (this figure). See also Figure S5, Data S5, and S6. Abbreviations: PC, phosphatidylcholine; PE, phosphatidylethanolamine; FFA, free fatty acid; SM, sphingomyelin; Hex2Cer, dihexosylceramides ; Cer, ceramide; TAG, triacylglycerol; DAG, diacylglycerol; LPE, lysophosphatidylethanolamine; CE, cholesteryl ester; LPC, lysophosphatidylcholine; HexCer, hexosylceramide; PA, phosphatidic acid; PG, phosphatidylglycerol; PGP, phosphatidylglycerolphosphate; PI, phosphatidylinositol; PS, phosphatidylserine.

spectrometric absolute quantitation of the lipidome (Data S5). The total lipid content in large cells was ~1.6x larger than in proliferating cells after normalization to total protein (Figure 5B).

Because ferroptosis sensitivity is strongly affected by lipid saturation,[34] we also included a sterol desaturase (SCD1) inhibitor CAY10566 in our lipidomic analysis. DMSO-, doxorubicin-, and CAY10566-treated samples clustered distinctly in principal-component analysis, primarily based on differences in triacylglycerides (TAGs) and phosphatidylcholine (PC) content (Figure S4A), indicating that desaturase inhibitor and doxorubicin modify the lipidome in distinct ways. Doxorubicin samples were different from CAY10566-treated cells in the unsaturation level of TAGs (Figure S4B), whereas the fatty acid chain length did not vary significantly between any of the three samples (Figure S4C).

The large doxorubicin-treated cells contained increased amounts of lipids known to be enriched in the ER,[36] including phosphatidylcholine (PC), ceramides (Cer; Hex2Cer), and lipophosphatidylcholine (LPC) (Figure 5C). Free fatty acids (FFAs) and triacylglycerides were also significantly elevated. Levels of free arachidonic acid and adrenic acid, which are main ferroptosis substrates were increased, whereas their phosphatidylethanolamine conjugates were not (Figure S4C). In general, the lipid saturation quantified as the ratio of polyunsaturated (PUFA) and monounsaturated fatty acids (MUFA) indicated no differences in

FFAs of specific length. In contrast, significant differences in saturation of phospholipids (PLs) were observed (Figures S4D and S4E). Thus, large doxorubicin-arrested cells display both lipid accumulation and remodeling.

To provide direct support for lipid peroxidation in large cells, we performed redox lipidomics to identify the oxidized lipid species (Figures S4F–S4H and Data S6). We treated control and doxorubicin-treated cells briefly with RSL3 to enhance the detection of oxidized lipids, as these would be otherwise suppressed by endogenous GPX4. This analysis identified 146 oxidized lipid species. The increased levels of oxidized lipids in large cells treated with RSL3 are consistent with the C11-Bodipy staining (see Figures 3C and 3D). Phosphatidylethanolamine (PE) species were especially affected by lipid peroxidation (Figures 5D–5F). For example, the known ferroptotic lipid marker PE(18:0/20:4)+3O[34] was substantially increased (Figure 5G).

To demonstrate the contribution of lipids to ferroptosis sensitivity, we tested the effect of exogenous lipids. Lipid-depleted serum in the culture medium sensitized both control and doxorubicin-treated cells (Figure 5H), indicating that serum-derived lipids protect from ferroptosis, whereas the endogenous cellular lipids do not. Conversely, adding oleic acid, a prototypic MUFA, fully protected both control and doxorubicin-treated cells (Figure 5I). Genetically, knocking out ACSL4, a gene responsible for generating oxidizable lipid substrates for ferroptosis, suppressed RSL3 sensitivity of large cells (Figure 5J). Overall, our data indicate that multiple factors including ER expansion, increased iron and lipid content, as well as lipid remodeling contribute to the ferroptosis sensitivity in large cells (Figure 5K).

Lipid peroxidation may contribute to cell size homeostasis and determination of an optimal cell size in proliferating cells

Cultured human cells maintain tight size homeostasis throughout the cell cycle, as evidenced by limited size variation around the mean size of the cell population.[11] The co-culture experiments with GPX4 KO cells (Figure 2G) indicated cell autonomous sensitization to ferroptosis in large cells. We asked if abnormally large cells within a proliferating population would display increased ferroptosis sensitivity, as this could have implications for cell size homeostasis and how an optimal cell size is determined. We first performed single-cell analysis by time-lapse imaging of RPE1 cells expressing mScarlet-PCNA (proliferating cell nuclear antigen) as a cell-cycle reporter and treated these cells with 200 nM palbociclib for 48 h. Three hours after palbociclib washout, approximately half of the cells had moved into S phase (Figures 6A and S6A). Using nuclear area as a proxy for cell size, the palbociclib-treated cells were on average ~50% larger than untreated cells in G1 (Figure 6A). Single-cell analysis further confirmed that ferroptosis sensitivity is not dependent on cell-cycle arrest. Palbociclib-treated cells in G1 and S phase died equally often after adding 100 nM GPX4 inhibitor ML162 as indicated by the shorter than full-length tracks (Figures 6B, S6A, Videos S1, and S2). We then quantified nuclear sizes in ML162-treated cells using deep-learning-based single-cell tracking,[37] as cell rounding induced by ferroptosis coincided with a decrease in nuclear area at the plane of view due to the deformation of the nucleus (Figures 6B and S6B). In palbociclib-treated cells, the average nuclear area started to reduce rapidly after ~3h (Figure 6C), consistent with holographic phase imaging (see Figure 3A). Larger cells also showed more pronounced changes in nuclear size in response to ML162 (Figure 6C). As a control, we used non-palbociclib-treated cells in G1 or S phase at the beginning of the experiment and excluded single-cell tracks that underwent cell division. A clear reduction in nuclear area was also observed in control cells larger than 200 μm^2 nuclear area (corresponding to ~90^{th} percentile of the nuclear size) (Figure 6C), indicating that this effect is not palbociclib dependent but related to the large cell size. The normal-sized control cells with an average nuclear area smaller than 200 μm^2 did not undergo ferroptosis, and their nuclear area progressively increased during the 7 h experiment as would be expected for cells growing and progressing through the cell cycle.

To quantify the effect of lipid peroxidation in GPX4-inhibited cells, we calculated the total variance in nuclear area during the experiment. Binned data revealed that a larger initial nuclear area led to increased variation in nuclear size after ML162 addition (Figure S6C). In particular, the 200–250 μm^2 bin, which is the first bin larger than most normal-sized G1 cells, had significantly increased nuclear size variation upon ML162 treatment consistent with the idea that abnormally large cells require GPX4 to prevent damage induced by endogenous lipid peroxidation. A trend of increasing variation in the 200–250 μm^2 bin was also evident in control cells without palbociclib, but this was not statistically significant due to the small number of abnormally large cells in untreated cultures.

The single-cell tracking data suggested that increased lipid peroxidation could change the cell size distribution of proliferating cell populations when treated with GPX4 inhibitors by selectively killing the largest cells. Based on this, we predicted that low concentrations of GPX4 inhibitors that do not kill the complete population will change the positive skewness of an unperturbed cell population to a more symmetrical cell size distribution, thus altering the size homeostasis (Figure 6D). Indeed, 100 nM RSL3 reduced the skewness of the cell size distribution in proliferating RPE1 cells as measured by coulter counter (Figure 6D). Quantification of the normalized cell counts in each 1 μm cell size bin between 20 and 30 μm cell diameter showed a progressive reduction in cell counts in GPX4-inhibited cells with increasing cell size as indicated by the negative slope of the regression lines (Figure S6D). Change in the skewness was dose dependent and inhibited by Fer-1 in both RPE1 and MDA-MB-231 cells (Figures 6E and 6F). Overall, this indicates that larger cells in proliferating populations are more susceptible to ferroptosis with potential implications to cell size homeostasis and determination of an optimal cell size of the population.

DISCUSSION

In this work, we identified how cell size alters the cellular fitness landscape by performing a computational genome-wide fitness analysis involving CRISPR/Cas9 KO data from tens of human cell lines. Although CRISPR/Cas9 screens have demonstrated that gene essentially can be context specific,[38] to our knowledge gene essentiality has never been associated with cell

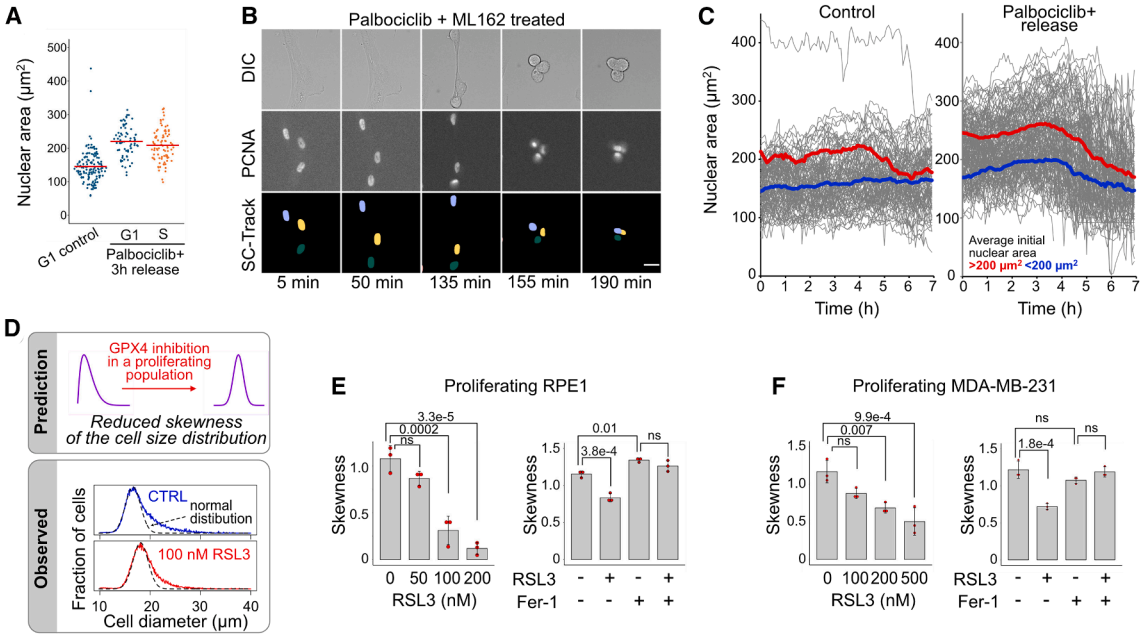

Figure 6. Preferential elimination of large than normal-sized cells from proliferating populations alters cell size homeostasis

(A) Nuclear area of proliferating G1 cells as well as G1 and S phase cells after 3 h of palbociclib release. The vertical red bars show mean nuclear size. n = 140, 72, and 86 for each group. RPE1-mScarlet-PCNA cells were treated with or without 200 nM palbociclib for 48 h.

(B) Differential interference contrast (DIC) images, PCNA fluorescence (PCNA) as well as the nuclei of the three cells treated with palbociclib and ML162 cells as identified by the tracking software (SC-Track) at the indicated times. Scale bar: 10 μm.

(C) Single cell traces of nuclear area changes in control and 2-day palbociclib-treated cells immediately after ML162 addition. Red and blue lines show the average behavior of cells with larger or smaller than 200 μm^2 nuclear size, respectively. The single large outlier cell in control sample was excluded from mean nuclear size calculations. n = 100 for control and 158 for palbociclib groups.

(D) Predicted and observed effect of RSL3 on cell size distribution in a proliferating cell population. Dashed black line overlaid with the observed cell sizes shows normal distribution. Note that swelling (see Figure 3B) shifts the size distribution slightly to the right.

(E) Skewness in RPE1 populations treated with varying concentrations of RSL3 (left) or combinations of RSL3 and Fer-1 (right).

(F) Skewness in MDA-MB-231 populations. For experiments with Fer-1, cells were cultured for 3 days with and without 1 μM Fer-1 and either 100 nM (for RPE1) or 500 nM (for MDA-MB-231) RSL3 was added for 24 h. Data shown are mean ± SD, n = 3. ANOVA followed by Tukey's post-hoc test. See also Figure S6 and Videos S1, and S2.

morphological factors, such as cell size. Our analysis revealed that essentiality of genes related to mitochondria and plasma membrane repair display cell-size-dependent changes. Although most of these changes are relatively modest, the quantitative nature of the analysis allowed us to predict that the change in the essentiality of GPX4, an enzyme that prevents membrane accumulation of deadly lipid hydroperoxides, is relevant with cell size ranges achievable in cultured cells. Furthermore, the change in essentiality of GPX4 was independent of a cell-cycle arrest and occurred also in non-cancerous cells. Therefore, inclusion of a sufficiently large and diverse set of cell lines in our fitness analysis not only generalizes the previously identified association of mitochondrial functionality with cell size in individual cell lines and mouse liver[7–9] but also allowed us to identify that larger cells have increased dependency for GPX4.

Although the computational analysis used multiple cell lines, the implications of these findings are likely to be more relevant for populations of the same cells. Specifically, our validation experiments demonstrate that growth beyond the optimal cell size sensitizes cells to oxidative membrane damage. Therefore, our genome-wide fitness analysis conceptually advances understanding of the importance of optimal cell size.[7] Although previous work has identified that RNA and protein synthesis becomes limiting for excessively large cells,[5] our analyses suggest that lipids may constrain cell size increase due to the damage caused by lipid peroxidation. Thus, RNA, proteins, and lipids all contribute to the necessity of carefully maintaining cell size within a narrow optimal range.[7,39,40] Of note, although protein and RNA synthesis limitations may be due to the increase in cytoplasm-to-DNA ratio,[5,31] it is not immediately obvious how this genome-dilution model could explain an increase in cellular lipid and iron content, the remodeling of the lipidome, and the resulting ferroptosis sensitivity.

Ferroptosis can be executed and regulated by a constellation of different mechanisms,[41] often with conflicting results in different genetic and cell biological contexts. For example, activation of p53 may induce, suppress, or have no effect on ferroptosis in different cell lines or different treatments.[42] This was also evident in our data, where p53 activation by nutlin-3 was variable in different cell-cycle gene knockout cell lines (see Figures S2F and S2G). Similarly, recent reports demonstrate that a cell-cycle arrest may coincide with ferroptosis sensitization[27] or resistance.[43] Similarly to our observations, ferroptosis sensitization was specific to GPX4 inhibition.[27] Our data suggest that a

primary driver for ferroptosis sensitization in these experiments is not a cell-cycle arrest but favoring cell growth (metabolism) over cell-cycle progression, a process that increases cell size.[44] Although it is challenging to compare results from different model systems, the up to 3,000-fold sensitization in RPE1 cells provides strong support for the importance of cell size in defining a ferroptosis-sensitive cell state.

Previous studies have indicated that changes in metabolism and mitochondrial function,[7–9,45] lipid amount and lipid composition,[34,35,46] as well as iron homeostasis[16,47] are contributing factors to a ferroptosis sensitive state.[41] Our proteomics and lipidomics data, imaging, and functional assays together provide a holistic cell biological explanation for the ferroptosis-sensitive state in large cells. These analyses revealed that ER, the primary site of lipid synthesis, expands more than proportionally to cell size (superscaling) in each cell-cycle phase, and this was accompanied by iron and lipid accumulation and lipid remodeling. We also confirmed that knocking out ACSL4, an enzyme that modulates lipid composition, rescues ferroptosis sensitivity as does preventing ER superscaling by relieving ER stress by IRE-1 inhibition and knockout. Lastly, iron chelation was more effective in suppressing ferroptosis in large cells, consistent with increased ER iron content observed by imaging and flow cytometry. Altogether, these findings highlight the multifactorial nature of ferroptosis sensitivity[41,42] and the importance of considering the cell biological context, including cell size.

Ferroptosis sensitization of abnormally large cells has also potential biomedical applications. As an example, senescent cells are characterized by large cell size.[4] Strategies that promote GPX4-inhibition-mediated ferroptosis could potentially be used for eliminating senescent cells. Senescence is not only observed in aging tissues but also in some cancers. Previous work has shown that "high mesenchymal-therapy-resistant" cancer cells depend on GPX4 for survival.[48,49] Despite the general toxicity of GPX4 inhibitors *in vivo*, the substantial sensitization of large cells might in some cases provide a sufficient therapeutic window to use GPX4 inhibitors as "ferro-senolytics" for aging and cancers.

Overall our data indicate that lipid peroxidation is a fitness cost for large cells highlighting the importance "on being of the right cell size."[39] Previous work suggest that deviating from the optimal cell size could cause small cells to die by apoptosis.[50] Similarly, ferroptosis could potentially limit overgrowth and help to maintain cell size homeostasis. This also hints to the possibility that iron-mediated oxidative damage and death may have played a role in shaping the evolution of cell size. Lenski's long-term evolution experiment shows that the clone that generates the largest bacteria is also the one most prone to die and uses citrate, an iron chelator, as the carbon source.[1] We can now speculate that in animals, evolution of cell size may have been constrained by membrane lipid peroxidation. Phylogenetic analysis places GPX4 as the most ancient member among the glutathione peroxidase family in vertebrates,[51] whereas clustering of animal GPX4 with plant and fungi sequences points to functional pressures during evolution.[52] Understanding the evolutionary pressures and potential constraints such as lipid peroxidation could therefore provide important insights into the evolution, functions, and physiological importance of both cell size and ferroptosis.

Limitations of the study

We provide evidence for association of ferroptosis sensitivity with cell size across tens of cancer cell lines and further generalize these findings by testing also non-cancerous cell lines, mainly RPE1 cells, but also HUVECs and IMR-90 fibroblasts. This study focused on cultured cells, but others have observed that palbociclib increases ferroptosis sensitivity *in vivo*.[27] The cell size range that is included in our analysis does not span the entire range of sizes observed in human cells[18] but still covers a large proportion of the sizes occupied by different cell types. We have concentrated our efforts on distinguishing between a cell-cycle arrest and cell size effect and identified contributors to the ferroptosis-sensitive state in large cells such as ER expansion, iron and lipid accumulation, and lipid remodeling. We focused on cell volume changes caused by increase in biomass and did not use changes in osmolarity for manipulating cell volume, as hypoosmotic treatments require dilution of the culture medium. For example, antioxidants and lipid content in FBS affects quantitative results and might even in extreme cases lead to contradictory outcomes in ferroptosis sensitivity. Conversely, although enlarged arrested cells could be treated with hyperosmotic stress to make the smaller, it is unclear how quickly such treatment would reverse ER expansion, iron content, and lipid peroxidation—or whether it would have any effect at all. Given the multiple ways how ferroptosis sensitivity can be altered in different model systems, ferroptosis induction by GPX4 inhibition is unlikely to be universally applicable approach to kill all large cells. Finally, because there is no molecular and cellular fossil record, any inference of this work on evolution of cell size and ferroptosis sensitivity is speculative.

RESOURCE AVAILABILITY

Lead contact

Further information and requests for resources and reagents should be directed to and will be fulfilled by the lead contact, Mikael Björklund (mikael.bjorklund.lab@gmail.com).

Materials availability

Cell lines and other materials generated in this study will be shared by the lead contact upon request.

Data and code availability

Public data sources used for analysis are described in STAR Methods. RNA-seq data have been deposited at the NCBI GEO repository (accession GSE261028). All other data can be found as supplemental information.

All other data generated or analyzed during this study are included in the main manuscript and the supplementary information files.

ACKNOWLEDGMENTS

We thank Yuchen Cheng and Jingyuan Chen for technical assistance and the Core Facilities at the Zhejiang University-University of Edinburgh Institute for instrumentation. This work was financially supported by funding from Zhejiang University and National Natural Science Foundation of China (grant number 31970706) to M.B. R.R.H. and F.W. are supported by National Science Foundation of China (grant numbers T2341004 and 82321004 as well as 32330047 and 31930057, respectively). R.Y. is supported by the dual award PhD degree program in Integrative Biomedical Sciences at Zhejiang University-University of Edinburgh Institute.

AUTHOR CONTRIBUTIONS

K.Y.C. designed, performed, and interpreted spinning disk and single-cell tracking experiments, provided resources and software tools, and edited the manuscript; Y.Y., Y.K., and L.C. performed specific experiments; R.Y., P.W., and P.S.Y.C. optimized methods and imaging tools; R.W., W.Y.S., and R.R. H. performed the redox lipidomics experiment; J.M. and F.W. participated in discussion and provided comments on the manuscript; M.B. conceptualized the study, performed formal analysis and investigation, supervised the study, and wrote the manuscript with input from K.Y.C.

DECLARATION OF INTERESTS

The authors declare no competing interests.

STAR★METHODS

Detailed methods are provided in the online version of this paper and include the following:

- KEY RESOURCES TABLE
- EXPERIMENTAL MODEL AND STUDY PARTICIPANT DETAILS
  - Cell lines
- METHOD DETAILS
  - External datasets
  - Cell size dependent fitness screen
  - Control screens
  - Ferroptosis induction
  - Cell size measurements
  - Senescence assay
  - Triglyceride assay
  - Lipid depletion
  - CRISRP-Cas9 knockouts
  - Lipid peroxidation by C11-Bodipy staining
  - Holographic and time-lapse imaging
  - Nuclear segmentation, cell cycle quantification and single cell lineage analysis
  - Imaging and flow cytometry quantification of the labile iron pool
  - Imaging and flow cytometry quantification with ER tracker
  - Absolute quantification of lipids
  - Redox phospholipidomics
  - RNAseq
  - Double palbociclib synchronization
  - Proteomics
  - Western blotting and immunofluorescence
- QUANTIFICATION AND STATISTICAL ANALYSIS

SUPPLEMENTAL INFORMATION

Supplemental information can be found online at https://doi.org/10.1016/j.isci.2025.112363.

Received: November 19, 2024
Revised: March 20, 2025
Accepted: April 2, 2025
Published: April 9, 2025

REFERENCES

1. Grant, N.A., Abdel Magid, A., Franklin, J., Dufour, Y., and Lenski, R.E. (2021). Changes in Cell Size and Shape during 50,000 Generations of Experimental Evolution with Escherichia coli. J. Bacteriol. *203*, e00469-20. https://doi.org/10.1128/JB.00469-20.
2. Lenski, R.E., and Travisano, M. (1994). Dynamics of adaptation and diversification: a 10,000-generation experiment with bacterial populations. Proc. Natl. Acad. Sci. USA *91*, 6808–6814. https://doi.org/10.1073/pnas.91.15.6808.
3. Lane, N., and Martin, W. (2010). The energetics of genome complexity. Nature *467*, 929–934. https://doi.org/10.1038/nature09486.
4. Hernandez-Segura, A., Nehme, J., and Demaria, M. (2018). Hallmarks of Cellular Senescence. Trends Cell Biol. *28*, 436–453. https://doi.org/10.1016/j.tcb.2018.02.001.
5. Neurohr, G.E., Terry, R.L., Lengefeld, J., Bonney, M., Brittingham, G.P., Moretto, F., Miettinen, T.P., Vaites, L.P., Soares, L.M., Paulo, J.A., et al. (2019). Excessive Cell Growth Causes Cytoplasm Dilution And Contributes to Senescence. Cell *176*, 1083–1097.e18. https://doi.org/10.1016/j.cell.2019.01.018.
6. Caldez, M.J., Van Hul, N., Koh, H.W.L., Teo, X.Q., Fan, J.J., Tan, P.Y., Dewhurst, M.R., Too, P.G., Talib, S.Z.A., Chiang, B.E., et al. (2018). Metabolic Remodeling during Liver Regeneration. Dev. Cell *47*, 425–438.e5. https://doi.org/10.1016/j.devcel.2018.09.020.
7. Miettinen, T.P., and Björklund, M. (2016). Cellular Allometry of Mitochondrial Functionality Establishes the Optimal Cell Size. Dev. Cell *39*, 370–382. https://doi.org/10.1016/j.devcel.2016.09.004.
8. Miettinen, T.P., and Björklund, M. (2017). Mitochondrial Function and Cell Size: An Allometric Relationship. Trends Cell Biol. *27*, 393–402. https://doi.org/10.1016/j.tcb.2017.02.006.
9. Miettinen, T.P., Pessa, H.K.J., Caldez, M.J., Fuhrer, T., Diril, M.K., Sauer, U., Kaldis, P., and Björklund, M. (2014). Identification of transcriptional and metabolic programs related to mammalian cell size. Curr. Biol. *24*, 598–608. https://doi.org/10.1016/j.cub.2014.01.071.
10. Secaira-Morocho, H., Chede, A., Gonzalez-de-Salceda, L., Garcia-Pichel, F., and Zhu, Q. (2024). An evolutionary optimum amid moderate heritability in prokaryotic cell size. Cell Rep. *43*, 114268. https://doi.org/10.1016/j.celrep.2024.114268.
11. Liu, X., Yan, J., and Kirschner, M.W. (2024). Cell size homeostasis is tightly controlled throughout the cell cycle. PLoS Biol. *22*, e3002453. https://doi.org/10.1371/journal.pbio.3002453.
12. Behan, F.M., Iorio, F., Picco, G., Gonçalves, E., Beaver, C.M., Migliardi, G., Santos, R., Rao, Y., Sassi, F., Pinnelli, M., et al. (2019). Prioritization of cancer therapeutic targets using CRISPR-Cas9 screens. Nature *568*, 511–516. https://doi.org/10.1038/s41586-019-1103-9.
13. Dempster, J.M., Pacini, C., Pantel, S., Behan, F.M., Green, T., Krill-Burger, J., Beaver, C.M., Younger, S.T., Zhivich, V., Najgebauer, H., et al. (2019). Agreement between two large pan-cancer CRISPR-Cas9 gene dependency data sets. Nat. Commun. *10*, 5817. https://doi.org/10.1038/s41467-019-13805-y.
14. Ghandi, M., Huang, F.W., Jané-Valbuena, J., Kryukov, G.V., Lo, C.C., McDonald, E.R., 3rd, Barretina, J., Gelfand, E.T., Bielski, C.M., Li, H., et al. (2019). Next-generation characterization of the Cancer Cell Line Encyclopedia. Nature *569*, 503–508. https://doi.org/10.1038/s41586-019-1186-3.
15. Dolfi, S.C., Chan, L.L.Y., Qiu, J., Tedeschi, P.M., Bertino, J.R., Hirshfield, K.M., Oltvai, Z.N., and Vazquez, A. (2013). The metabolic demands of cancer cells are coupled to their size and protein synthesis rates. Cancer Metab. *1*, 20. https://doi.org/10.1186/2049-3002-1-20.
16. Stockwell, B.R., Friedmann Angeli, J.P., Bayir, H., Bush, A.I., Conrad, M., Dixon, S.J., Fulda, S., Gascón, S., Hatzios, S.K., Kagan, V.E., et al. (2017). Ferroptosis: A Regulated Cell Death Nexus Linking Metabolism, Redox Biology, and Disease. Cell *171*, 273–285. https://doi.org/10.1016/j.cell.2017.09.021.
17. Tang, D., Chen, X., Kang, R., and Kroemer, G. (2021). Ferroptosis: molecular mechanisms and health implications. Cell Res. *31*, 107–125. https://doi.org/10.1038/s41422-020-00441-1.
18. Hatton, I.A., Galbraith, E.D., Merleau, N.S.C., Miettinen, T.P., Smith, B.M., and Shander, J.A. (2023). The human cell count and size distribution. Proc. Natl. Acad. Sci. USA *120*, e2303077120. https://doi.org/10.1073/pnas.2303077120.

19. Li, H., Ning, S., Ghandi, M., Kryukov, G.V., Gopal, S., Deik, A., Souza, A., Pierce, K., Keskula, P., Hernandez, D., et al. (2019). The landscape of cancer cell line metabolism. Nat. Med. *25*, 850–860. https://doi.org/10.1038/s41591-019-0404-8.

20. Han, S., Lee, M., Shin, Y., Giovanni, R., Chakrabarty, R.P., Herrerias, M. M., Dada, L.A., Flozak, A.S., Reyfman, P.A., Khuder, B., et al. (2023). Mitochondrial integrated stress response controls lung epithelial cell fate. Nature *620*, 890–897. https://doi.org/10.1038/s41586-023-06423-8.

21. Dai, E., Meng, L., Kang, R., Wang, X., and Tang, D. (2020). ESCRT-III-dependent membrane repair blocks ferroptosis. Biochem. Biophys. Res. Commun. *522*, 415–421. https://doi.org/10.1016/j.bbrc.2019.11.110.

22. Yasuda-Yamahara, M., Rogg, M., Frimmel, J., Trachte, P., Helmstaedter, M., Schroder, P., Schiffer, M., Schell, C., and Huber, T.B. (2018). FERMT2 links cortical actin structures, plasma membrane tension and focal adhesion function to stabilize podocyte morphology. Matrix Biol. *68–69*, 263–279. https://doi.org/10.1016/j.matbio.2018.01.003.

23. Haney, M.S., Bohlen, C.J., Morgens, D.W., Ousey, J.A., Barkal, A.A., Tsui, C.K., Ego, B.K., Levin, R., Kamber, R.A., Collins, H., et al. (2018). Identification of phagocytosis regulators using magnetic genome-wide CRISPR screens. Nat. Genet. *50*, 1716–1727. https://doi.org/10.1038/s41588-018-0254-1.

24. Kagan, V.E., Mao, G., Qu, F., Angeli, J.P.F., Doll, S., Croix, C.S., Dar, H.H., Liu, B., Tyurin, V.A., Ritov, V.B., et al. (2017). Oxidized arachidonic and adrenic PEs navigate cells to ferroptosis. Nat. Chem. Biol. *13*, 81–90. https://doi.org/10.1038/nchembio.2238.

25. Cheff, D.M., Huang, C., Scholzen, K.C., Gencheva, R., Ronzetti, M.H., Cheng, Q., Hall, M.D., and Arnér, E.S.J. (2023). The ferroptosis inducing compounds RSL3 and ML162 are not direct inhibitors of GPX4 but of TXNRD1. Redox Biol. *62*, 102703. https://doi.org/10.1016/j.redox.2023.102703.

26. Yang, L., Wang, H., Yang, X., Wu, Q., An, P., Jin, X., Liu, W., Huang, X., Li, Y., Yan, S., et al. (2020). Auranofin mitigates systemic iron overload and induces ferroptosis via distinct mechanisms. Signal Transduct. Target. Ther. *5*, 138. https://doi.org/10.1038/s41392-020-00253-0.

27. Rodencal, J., Kim, N., He, A., Li, V.L., Lange, M., He, J., Tarangelo, A., Schafer, Z.T., Olzmann, J.A., Long, J.Z., et al. (2024). Sensitization of cancer cells to ferroptosis coincident with cell cycle arrest. Cell Chem. Biol. *31*, 234–248.e13. https://doi.org/10.1016/j.chembiol.2023.10.011.

28. Riegman, M., Sagie, L., Galed, C., Levin, T., Steinberg, N., Dixon, S.J., Wiesner, U., Bradbury, M.S., Niethammer, P., Zaritsky, A., and Overholtzer, M. (2020). Ferroptosis occurs through an osmotic mechanism and propagates independently of cell rupture. Nat. Cell Biol. *22*, 1042–1048. https://doi.org/10.1038/s41556-020-0565-1.

29. Hirata, Y., Cai, R., Volchuk, A., Steinberg, B.E., Saito, Y., Matsuzawa, A., Grinstein, S., and Freeman, S.A. (2023). Lipid peroxidation increases membrane tension, Piezo1 gating, and cation permeability to execute ferroptosis. Curr. Biol. *33*, 1282–1294.e5. https://doi.org/10.1016/j.cub.2023.02.060.

30. Ogrodnik, M., Carlos Acosta, J., Adams, P.D., d'Adda di Fagagna, F., Baker, D.J., Bishop, C.L., Chandra, T., Collado, M., Gil, J., Gorgoulis, V., et al. (2024). Guidelines for minimal information on cellular senescence experimentation in vivo. Cell *187*, 4150–4175. https://doi.org/10.1016/j.cell.2024.05.059.

31. Lanz, M.C., Zatulovskiy, E., Swaffer, M.P., Zhang, L., Ilerten, I., Zhang, S., You, D.S., Marinov, G., McAlpine, P., Elias, J.E., and Skotheim, J.M. (2022). Increasing cell size remodels the proteome and promotes senescence. Mol. Cell *82*, 3255–3269.e8. https://doi.org/10.1016/j.molcel.2022.07.017.

32. von Krusenstiern, A.N., Robson, R.N., Qian, N., Qiu, B., Hu, F., Reznik, E., Smith, N., Zandkarimi, F., Estes, V.M., Dupont, M., et al. (2023). Identification of essential sites of lipid peroxidation in ferroptosis. Nat. Chem. Biol. *19*, 719–730. https://doi.org/10.1038/s41589-022-01249-3.

33. Cross, B.C.S., Bond, P.J., Sadowski, P.G., Jha, B.K., Zak, J., Goodman, J. M., Silverman, R.H., Neubert, T.A., Baxendale, I.R., Ron, D., and Harding, H.P. (2012). The molecular basis for selective inhibition of unconventional mRNA splicing by an IRE1-binding small molecule. Proc. Natl. Acad. Sci. USA *109*, E869–E878. https://doi.org/10.1073/pnas.1115623109.

34. Pope, L.E., and Dixon, S.J. (2023). Regulation of ferroptosis by lipid metabolism. Trends Cell Biol. *33*, 1077–1087. https://doi.org/10.1016/j.tcb.2023.05.003.

35. Oh, S., Lee, C., Yang, W., Li, A., Mukherjee, A., Basan, M., Ran, C., Yin, W., Tabin, C.J., Fu, D., et al. (2022). Protein and lipid mass concentration measurement in tissues by stimulated Raman scattering microscopy. Proc. Natl. Acad. Sci. USA *119*, e2117938119. https://doi.org/10.1073/pnas.2117938119.

36. van Meer, G., Voelker, D.R., and Feigenson, G.W. (2008). Membrane lipids: where they are and how they behave. Nat. Rev. Mol. Cell Biol. *9*, 112–124. https://doi.org/10.1038/nrm2330.

37. Li, C., Xie, S.S., Wang, J., Sharvia, S., and Chan, K.Y. (2024). SC-Track: a robust cell-tracking algorithm for generating accurate single-cell lineages from diverse cell segmentations. Brief. Bioinform. *25*, bbae192. https://doi.org/10.1093/bib/bbae192.

38. Hart, T., Chandrashekhar, M., Aregger, M., Steinhart, Z., Brown, K.R., MacLeod, G., Mis, M., Zimmermann, M., Fradet-Turcotte, A., Sun, S., et al. (2015). High-Resolution CRISPR Screens Reveal Fitness Genes and Genotype-Specific Cancer Liabilities. Cell *163*, 1515–1526. https://doi.org/10.1016/j.cell.2015.11.015.

39. Ginzberg, M.B., Kafri, R., and Kirschner, M. (2015). Cell biology. On being the right (cell) size. Science *348*, 1245075. https://doi.org/10.1126/science.1245075.

40. Miettinen, T.P., Caldez, M.J., Kaldis, P., and Björklund, M. (2017). Cell size control - a mechanism for maintaining fitness and function. Bioessays *39*. https://doi.org/10.1002/bies.201700058.

41. Dixon, S.J., and Pratt, D.A. (2023). Ferroptosis: A flexible constellation of related biochemical mechanisms. Mol. Cell *83*, 1030–1042. https://doi.org/10.1016/j.molcel.2023.03.005.

42. Dixon, S.J., and Olzmann, J.A. (2024). The cell biology of ferroptosis. Nat. Rev. Mol. Cell Biol. *25*, 424–442. https://doi.org/10.1038/s41580-024-00703-5.

43. Lee, H., Horbath, A., Kondiparthi, L., Meena, J.K., Lei, G., Dasgupta, S., Liu, X., Zhuang, L., Koppula, P., Li, M., et al. (2024). Cell cycle arrest induces lipid droplet formation and confers ferroptosis resistance. Nat. Commun. *15*, 79. https://doi.org/10.1038/s41467-023-44412-7.

44. Bjorklund, M. (2019). Cell size homeostasis: Metabolic control of growth and cell division. Biochim. Biophys. Acta Mol. Cell Res. *1866*, 409–417. https://doi.org/10.1016/j.bbamcr.2018.10.002.

45. Wiley, C.D., Velarde, M.C., Lecot, P., Liu, S., Sarnoski, E.A., Freund, A., Shirakawa, K., Lim, H.W., Davis, S.S., Ramanathan, A., et al. (2016). Mitochondrial Dysfunction Induces Senescence with a Distinct Secretory Phenotype. Cell Metab. *23*, 303–314. https://doi.org/10.1016/j.cmet.2015.11.011.

46. Lizardo, D.Y., Lin, Y.L., Gokcumen, O., and Atilla-Gokcumen, G.E. (2017). Regulation of lipids is central to replicative senescence. Mol. Biosyst. *13*, 498–509. https://doi.org/10.1039/c6mb00842a.

47. Maus, M., López-Polo, V., Mateo, L., Lafarga, M., Aguilera, M., De Lama, E., Meyer, K., Sola, A., Lopez-Martinez, C., López-Alonso, I., et al. (2023). Iron accumulation drives fibrosis, senescence and the senescence-associated secretory phenotype. Nat. Metab. *5*, 2111–2130. https://doi.org/10.1038/s42255-023-00928-2.

48. Hangauer, M.J., Viswanathan, V.S., Ryan, M.J., Bole, D., Eaton, J.K., Matov, A., Galeas, J., Dhruv, H.D., Berens, M.E., Schreiber, S.L., et al. (2017). Drug-tolerant persister cancer cells are vulnerable to GPX4 inhibition. Nature *551*, 247–250. https://doi.org/10.1038/nature24297.

49. Viswanathan, V.S., Ryan, M.J., Dhruv, H.D., Gill, S., Eichhoff, O.M., Seashore-Ludlow, B., Kaffenberger, S.D., Eaton, J.K., Shimada, K., Aguirre, A.J., et al. (2017). Dependency of a therapy-resistant state of

cancer cells on a lipid peroxidase pathway. Nature *547*, 453–457. https://doi.org/10.1038/nature23007.

50. Aryaman, J., Hoitzing, H., Burgstaller, J.P., Johnston, I.G., and Jones, N.S. (2017). Mitochondrial heterogeneity, metabolic scaling and cell death. Bioessays *39*. https://doi.org/10.1002/bies.201700001.

51. Mariotti, M., Ridge, P.G., Zhang, Y., Lobanov, A.V., Pringle, T.H., Guigo, R., Hatfield, D.L., and Gladyshev, V.N. (2012). Composition and evolution of the vertebrate and mammalian selenoproteomes. PLoS One *7*, e33066. https://doi.org/10.1371/journal.pone.0033066.

52. Margis, R., Dunand, C., Teixeira, F.K., and Margis-Pinheiro, M. (2008). Glutathione peroxidase family - an evolutionary overview. FEBS J. *275*, 3959–3970. https://doi.org/10.1111/j.1742-4658.2008.06542.x.

53. Meyers, R.M., Bryan, J.G., McFarland, J.M., Weir, B.A., Sizemore, A.E., Xu, H., Dharia, N.V., Montgomery, P.G., Cowley, G.S., Pantel, S., et al. (2017). Computational correction of copy number effect improves specificity of CRISPR-Cas9 essentiality screens in cancer cells. Nat. Genet. *49*, 1779–1784. https://doi.org/10.1038/ng.3984.

54. Sheltzer, J.M. (2013). A transcriptional and metabolic signature of primary aneuploidy is present in chromosomally unstable cancer cells and informs clinical prognosis. Cancer Res. *73*, 6401–6412. https://doi.org/10.1158/0008-5472.CAN-13-0749.

55. Zielinski, D.C., Jamshidi, N., Corbett, A.J., Bordbar, A., Thomas, A., and Palsson, B.O. (2017). Systems biology analysis of drivers underlying hallmarks of cancer cell metabolism. Sci. Rep. *7*, 41241. https://doi.org/10.1038/srep41241.

56. Eden, E., Navon, R., Steinfeld, I., Lipson, D., and Yakhini, Z. (2009). GOrilla: a tool for discovery and visualization of enriched GO terms in ranked gene lists. BMC Bioinf. *10*, 48. https://doi.org/10.1186/1471-2105-10-48.

57. Gui, Y., Xie, S., Wang, Y., Wang, P., Yao, R., Gao, X., Dong, Y., Wang, G., and Chan, K.Y. (2022). pcnaDeep: a fast and robust single-cell tracking method using deep-learning mediated cell cycle profiling. Bioinformatics *38*, 4846–4847. https://doi.org/10.1093/bioinformatics/btac602.

58. Schmidt, U., Weigert, M., Broaddus, C., and Myers, G. (2018). Cell Detection with Star-Convex Polygons (Springer International Publishing), pp. 265–273. held in Cham.

59. Sun, W.Y., Wang, R., and He, R.R. (2023). LC-MS-Based Redox Phosphoipidomics Analysis in Ferroptosis. Methods Mol. Biol. *2712*, 81–90. https://doi.org/10.1007/978-1-0716-3433-2_8.

60. Sun, W.Y., Tyurin, V.A., Mikulska-Ruminska, K., Shrivastava, I.H., Anthonymuthu, T.S., Zhai, Y.J., Pan, M.H., Gong, H.B., Lu, D.H., Sun, J., et al. (2021). Phospholipase iPLA(2)beta averts ferroptosis by eliminating a redox lipid death signal. Nat. Chem. Biol. *17*, 465–476. https://doi.org/10.1038/s41589-020-00734-x.

STAR★METHODS

KEY RESOURCES TABLE

REAGENT or RESOURCE	SOURCE	IDENTIFIER
Antibodies		
anti-ACSL4	Abcam	ab155282; RRID:AB_2714020
anti-DHODH	Proteintech	14877-1-AP; RRID:AB_2091723
anti-FSP1	ProteinTech	20886-1-AP; RRID:AB_2878756
anti-GCH1	Proteintech	28501-1-AP; RRID:AB_2881157
anti-GAPDH	Genscript	A01622; RRID:AB_2622160
anti-GPX4	Abcam	ab125066; RRID:AB_10973901
anti-p21	Proteintech	10355-1-Ap; RRID:AB_2934700
anti-RB1	Cell Signaling Technology	9309; RRID:AB_823629
anti-RTN4	Proteintech	10740-1-AP; RRID:AB_2183598
anti-CALR	ZenBio	R380959
anti-REEP5	ABclonal	A10392; RRID:AB_2757940
anti-HMGB1	Cell Signaling Technology	6893; RRID:AB_10827882
anti-LMNB1	Cell Signaling Technology	17416; RRID:AB_3095982
anti-Ki67	Beyotime	AF1738; RRID:AB_3094450
anti-b-Actin	Genscript	A00702; RRID:AB_914102
Donkey Anti-Rabbit IgG (H&L) Alexa Fluor 555	Abcam	ab150074; RRID:AB_2636997
Goat anti-Mouse IgG (H + L) Alexa Fluor Plus 680	Thermo Fisher Scientific	A32729; RRID:AB_2633278
Goat anti-Rabbit IgG (H + L) Alexa Fluor Plus 800	Thermo Fisher Scientific	A32735; RRID:AB_2633284
Chemicals, peptides, and recombinant proteins		
RSL3	SigmaAldrich	SML2234; CAS: 1219810-16-8
Ferrostatin-1	SigmaAldrich	SML0583; CAS: 347174-05-4
Doxorubicin	Beyotime	SC0159; CAS: 25316-40-9
Palbociclib	SigmaAldrich	PZ0199; CAS: 827022-33-3
Erastin	SelleckChem	S7242; CAS: 571203-78-6
S-trityl-L-cysteine (STLC)	Aladdin	T101029; CAS: 2799-07-7
Bodipy 581/591 C11	Thermo Fisher Scientific	D3861
FerroOrange	Dojindo	F374
FerroFarRed/FeRhoNox-1	GLPBio	GC20134; CAS: 1447815-38-4
Liproxstatin-1	TargetMol	T2376; CAS: 950455-15-9
Barasertib	TargetMol	T2602; CAS: 722544-51-6
Deferoxamine mesylate	SigmaAldrich	D9533; CAS: 138-14-7
Vitamin E/a-tocopherol	SelleckChem and GLPBio	S6104 or GC41617; CAS: 10191-41-0
Z-VAD-FMK	SelleckChem	S7023
Necrostatin-1	TargetMol	T1847; CAS: 4311-88-0
MitoQuinone	GLPBio	GC30416; CAS: 444890-41-9
MitoQuinol	GLPBio	GC44205; CAS: 845959-55-9
CAY10566	TargetMol	T14878; CAS: 944808-88-2
ML162	SigmaAldrich	SML2561; CAS: 1035072-16-2
FIN56	Targetmol	T4066; CAS: 1083162-61-1
Sulfasalazine	TargetMol	T0907; CAS: 599-79-1
Auranofin	TargetMol	T1303; CAS: 34031-32-8
TRi-1	TargetMol	T5481; CAS: 246020-68-8
TOFA	TargetMol	T3988; CAS: 54857-86-2
STF-083010	MedChemExpress	HY-15845; CAS: 307543-71-1

(*Continued on next page*)

Continued

REAGENT or RESOURCE	SOURCE	IDENTIFIER
Doxycycline hyclate	SolarBio	D8960; CAS: 24390-14-5
Critical commercial assays		
CellTiter-Glo 2.0	Promega	G9243
Triglyceride-Glo	Promega	J3161
Senescence associated β-Galactosidase Staining Kit	Beyotime	C0602
Deposited data		
Computational cell size fitness analysis	This study	Data S1
Computational CNV and drug effect analysis	This study	Data S2
Cell size and cell cycle proteomics data	This study	Data S3
RNA sequencing data	This study; Gene Expression Omnibus	Data S4; GEO: GSE261028
Total lipidomics data	This study	Data S5
Redox lipidomics data	This study	Data S6
Experimental models: Cell lines		
hTERT-RPE1	ATCC	CRL-4000; RRID: CVCL_4388
HepG2	ATCC	HB-8065; RRID:CVCL_0027
IMR90	ATCC	CCL-186; RRID:CVCL_0347
A549	ATCC	CCL-185; RRID:CVCL_0023
CAKI1	ATCC	HTB-46; RRID:CVCL_0234
MDA-MB-231 (TCHu227)	Cell Bank of Chinese Academy of Science (Shanghai, China)	RRID:CVCL_0062
HUVEC	Zhejiang Meisen Cell Technology (Zhejiang, China)	#N/A
RPE1 GPX4 KO	This study	#N/A
RPE1 RB1 KO	This study	#N/A
RPE1 p21 KO	This study	#N/A
RPE1 ACSL4 KO	This study	#N/A
RPE1 IRE1 KO	This study	#N/A
RPE1 inducible mGreenLantern-p21-AAVS1	This study	#N/A
Oligonucleotides		
GPX4 sgRNA CTTGGCGGAAAACTCGTGCA and TTAACCTGGACAAGTACCGG	Tsingke	#N/A
ACSL4 sgRNA ACCTGGTCAGAGAGTGTAAG and GCATCATCACTCCCTTAGGT	Tsingke	#N/A
IRE1 sgRNA TCTCCCTCAATGGTACACGA	Tsingke	#N/A
RB1 sgRNA AAACAATCAAAGGACCGAGA and AACATCTAATGGACTTCCAG	Tsingke	#N/A
non-targeting control sgRNA TGAGCATT CGTAGCCCAGCA	Tsingke	#N/A
p21 sgRNA GGCGCCATGTCAGAACCGGC and GACAGCAGAGGAAGACCATG	Tsingke	#N/A
ATP1A1 sgRNA GAGTTCTGTAATTCAGCATA	Tsingke	#N/A
Recombinant DNA		
pLentiCRISPRv2	Addgene	#52961; RRID: Addgene_52961
Software and algorithms		
R version 4.3.2	The R Project for Statistical Computing	https://www.r-project.org/
scikit-image version 0.22.0	The scikit-image Development Team	https://scikit-image.org/
String version 12.0	String Consortium	https://string-db.org/
Holomonitor App suite version 4.0.1	Phase Holographic Imaging PHI AB	https://phiab.com/holomonitor/cell-imaging-software/

(*Continued on next page*)

Continued

REAGENT or RESOURCE	SOURCE	IDENTIFIER
StarDist	Github	https://github.com/stardist/stardist
SC-Track version 0.0.9	Github	https://github.com/chan-labsite/SC-Track
Fiji version 1.54	ImageJ	https://imagej.net/software/fiji/

EXPERIMENTAL MODEL AND STUDY PARTICIPANT DETAILS

Cell lines

hTERT-RPE1 (female), HepG2 (male), IMR90 (female), A549 (male) and CAKI1 (male) cells were obtained from ATCC. MDA-MB-231 (female) cells were from obtained from the Cell Bank of Chinese Academy of Sciences (Shanghai, China). HUVEC (gender/sex not available) cells were purchased from Zhejiang Meisen Cell Technology.

RPE1 cells were cultured in DMEM (SigmaAldrich, Cat.No. D5796 or Beijing Transgenbiotech, Cat.No. FI101-01) containing 25 mM Glucose, 10% FBS and penicillin-streptomycin. HepG2 and IMR90 cells in Eagle's Minimum Essential Medium 10% FBS and penicillin-streptomycin. A549 and CAKI1 cells in RMPI-1640 (HyClone, SH30096.FS) with 5% FBS and penicillin-streptomycin at 37°C with 5% CO_2. Cell line authentication was performed by the suppliers.

METHOD DETAILS

External datasets

Gene essentiality scores were downloaded from Broad Institute's DepMap portal (https://depmap.org/portal/download/). The DepMap Public 22Q2 version of the file *Achilles_gene_effect.csv* was used. The CERES scores describing the gene essentiality in each tested cell line, including 32 cell lines from the NCI60 collection, have been controlled for copy number variation, which is a major source of false positives in CRISPR-Cas9 KO screens.[53] These CERES scores have been further scaled and normalized so that the median of common essential genes in each cell lines equals −1. Therefore, the gene essentiality scores can be used directly without further data processing. Cell diameters as well as modal chromosome number (used for ploidy analysis), doubling time and NCI60 cells have been previously described.[15,54] The cell volumes are estimated from image-based measurements of cell diameters obtained after trypsin treatment of adherent cell lines. We assume that the cells are spherical after trypsin treatment and therefore cell volume can be approximated as $V = 4/3\pi(d/2)^3$, where d is the average diameter reported. The sustainable dry mass was obtained through computational reconstruction of human metabolic network and flux balance analysis.[55] Average growth rate for each cell line was calculated by dividing population cell volume with population doubling time.

Cell size dependent fitness screen

The publicly available Achilles_gene_effect.csv file from DepMap, and a phenotype file containing the cell volume information were used for establishing the linear models. All available datapoints were included in the analysis. Note that higher CERES score indicates lower essentiality. For cell size, we used log10 values of the cell volumes as logarithmic scale treats cell size variation as relative rather than absolute scale. This is because multiplicative(relative) error rather than absolute error is the appropriate way to treat variation in most growth-related models. Cell lines present on both gene essentiality score and phenotype files were selected and ordered alphabetically by cell line identification (DepMap_ID) for the linear regression analysis. Linear models with cell size were iteratively applied across all gene essentiality scores. T statistic, slope and *p* value for the regression model were extracted using lm(CERES ~ log10CellVolume)$coefficients[2,3], lm(CERES ~ log10CellVolume)$coefficients[2,1] and lm(CERES ~ log10CellVolume)$coefficients[2,4], respectively. We note that nonlinear relationships between phenotype and gene essentiality may exist, we reasoned that the use of a linear model is the simplest and computationally most efficient solution for finding most genes contributing to the phenotype. Gene Ontology analysis was performed using GOrilla.[56] Data was plotted using *ggplot2* (v. 3.5.0) and *ggpubr* (v. 0.6.0) packages in R or using Microsoft Excel.

Control screens

All control screens were performed in an identical manner to the original cell size screen. For gene copy number screen, the data in the CCLE_gene_cn.csv file (DepMap Public 20Q4) was used. For associating cell size with drug sensitivity screen, data in the Drug_sensitivity_(PRISM_Repurposing_Primary_Screen)_19Q4.csv file were used. Randomized screens were performed by randomly assigning cell volume measurements to the cell lines, calculating the t statistics and repeating the process for 10 000 times GPX4 and 1000 times for OxpPhos Complex I without replacement. For each iteration, the median for the t statistic value for OxpPhos Complex I subunit genes were calculated and the distribution of the median t statistic was plotted as histogram. This analysis was performed on the BIT BIO High-Performance Analyzing Platform (v2.0, Nanjing Baiaoyin Big Data Technology Co., Ltd.) with R version 3.6.2.

Ferroptosis induction

Ferroptosis was induced using 1S,3R-RSL3. For the rescue of ferroptosis, 1 μM ferrostatin-1, 1 μM alpha-tocopherol or 20 μM apoptosis inhibitor Z-VAD-FMK were used. To measure ferroptosis sensitivity, 2.5×10^4 cells/mL were plated on white 96-well plates (Costar, CatNo. 3917) in the presence or absence of 50 nM topoisomerase inhibitor doxorubicin or 1 μM CDK4/6 inhibitor Palbociclib for 3 days to increase cell size. After 3 days, fresh medium without doxorubicin and palbociclib but including RSL3 in 3-fold dilutions (9 dilutions and DMSO control) in the presence of absence of 1 μM Fer-1 was added for 24 h. Cell viability was measured based on cellular ATP levels using CellTiter-Glo 2.0 Assay (Promega, G9242) by adding 50 μL reagent per well followed by luminescence measurement using Tecan Spark multimode reader. The dose response model was fitted for the mean luminescence values using the *drm* function with four-parameter log-logistic model (LL.4) of the *drc* package (v. 3.0–1) in R. All cell-based experiments were performed with 3 replicates and experiments were repeated at least two times. For phase contrast imaging of cell death, cells were plated on 6 or 12-well plates and treated with doxorubicin or palbociclib for 3 days and treated with RSL3 with or without 1 μM ferrostatin-1, 1 μM alpha-tocopherol or 20 μM Z-VAD-FMK. Images were taken 24 h after RSL3 addition using Etaluma LS620 microscope.

For cell size manipulation by contact inhibition, 1 μM palbociclib treated cells incubated at 0.25 × 10e5/mL or 2 × 10e5/mL (contact inhibition) for 3 days, resulting in large and small G1 arrested cells. Then cells counted and plated for 16h in 0.5 × 10e5/mL density on white 96-well plates or 6 well plate for cell size measurement. RSL3 was added in 3-fold dilutions in fresh medium without palbociclib for 24h and assayed with CellTiter-Glo.

For testing the cell autonomous effect in a co-culture model, WT and GPX4 KO cells were trypsinized and washed once with HBSS. Cells were stained by adding 10 μM final concentration of CellTracker Green CMFDA (Yeasen) for WT cells and 10 μM CellTrace DeepRed for GPX4 KO cells and incubated at 37C for 30 min. The cells were then washed with PBS, counted and mixed in 1:1 ratio. 30 000 cells/mL were plated in a 12 well plate in complete medium with 1 μM Fer-1 and allowed to adhere for 4h. 15 Gy of X-ray irradiation with Rad Source RS2000pro-225 was used to induce cell-cycle arrest and make large cells. After incubating for 3days, Fer-1 was either washed away or maintained. Green and red fluorescent cells were counted manually under fluorescent microscope after 24 h.

Cell size measurements

To measure cell size, cells were trypsinized with TrypLE Express (Thermo-Fisher, 12604021) and cell size measured by Multisizer 4e Coulter Counter (Beckman Coulter) by adding the trypsinized cells to Isoton II electrolyte diluent. Measurements were performed on a 10–40 μm size range split into 400 bins. Mean, median size and skewness were used as reported by the Multisizer software. To compare cell death as a function of cell size in proliferating cell populations, the relative cell numbers from coulter counter data were binned with a 1um bin size. Log2 fold change compared to DMSO treated samples in each bin were calculated and the resulting datapoints fitted with linear model.

Alternatively, an image-based method using Countstar BioTech Automated Cell Counter (ALIT Life Science, Shanghai, China) was used. The average cell diameter was obtained from trypsinized cells mixed with an equal volume of 0.2% Trypan Blue in PBS as viability dye. Cell volumes were obtained from diameter by assuming a spherical morphology $V = 4/3\pi(d/2)^3$.

Senescence assay

The RPE1 mGreenLantern-p21 cells were established by cloning mGreenLantern in frame with p21 coding sequence into AAVS1-Tet plasmid (Addgene plasmid #158663, a kind gift from Masato Kanemaki). Stable transfectants integrated into the AAVS1 safe harbor locus were selected with puromycin. To induce cell-cycle arrest, mGreenLantern-p21 was induced with 1 μg/mL doxycycline for 3 days. Parallel cultures were then either measured by coulter counter, lysed and analyzed by western blotting, or fixed and stained for senescence associated-β-galactosidase activity (Beyotime).

Triglyceride assay

For measuring triglyceride levels in RPE1 cells, Triglyceride-Glo Assays was used (Promega, J3160). Briefly, RPE1 cells were plated at 0.5×10^5/mL and incubated with and without 50 nM doxorubicin in triplicates for 3 days. Cells were trypsinized, cell size and number was determined after which cell concentration was adjusted to 1×10^5/mL in PBS and samples assayed as per manufacturer's instructions. Luminescence was measured with Tecan Spark microplate reader and data normalized to cell volume.

Lipid depletion

FBS was depleted of lipids using di-isopropyl ether:n-butanol (0.8vol:0.2vol) by stirring for 30 min at room temperature. The extraction was centrifuged at 4,000 × g for 15 min at 4°C to separate FBS and the organic phase. The lower FBS phase was further extracted with equal volume of di-isopropyl ether for 30 min at room temperature and centrifuged as before. The lower phase was dialyzed overnight against 0.9% saline at 4°C and sterile filtered. Control FBS was dialyzed in parallel without organic extraction.

CRISRP-Cas9 knockouts

Knockout cell lines were generated by transfecting RPE1 cells with pLentiCRISPRv2 (a gift from Feng Zhang, Addgene, #52961; RRID: Addgene_52961) containing the sgRNAs for GPX4 (CTTGGCGGAAAACTCGTGCA and TTAACCTGGACAAGTACCGG), ACSL4 (ACCTGGTCAGAGAGTGTAAG and GCATCATCACTCCCTTAGGT), IRE1 (TCTCCCTCAATGGTACACGA), and RB1

(AAACAATCAAAGGACCGAGA and AACATCTAATGGACTTCCAG), as well as non-targeting control sgRNA (TGAGCATTCGTA GCCCAGCA). Puromycin selection was started 24 h after transfection and continued for 7 days after which the selection medium was replaced with normal culture medium, and the cells cultured for 2–3 days before limiting dilution in a 96-well plate. Wells with single clones were expanded and sgRNA target region sequenced. The p21 knockout was generated by deleting part of the ORF of p21 using a pair of sgRNAs (GGCGCCATGTCAGAACCGGC and GACAGCAGAGGAAGACCATG) co-transfected with a third sgRNA (GAGTTCTGTAATTCAGCATA) targeting ATP1A1 to allow co-selection with ouabain. Ouabain selection (100 μM) was started 48 h after transfection and continued for 7 days after which the selection medium was replaced with normal culture medium. Single cell clones were obtained by limiting dilution and western blotting used to confirm the knockout.

Lipid peroxidation by C11-Bodipy staining

Lipid peroxidation was measured by Bodipy-C11 staining. Briefly, cells were treated with palbociclib or doxorubicin for 3 days on a 6 well plate, starting with 1×10^5 cells/mL. Lipid peroxidation was induced with 1 μM RSL3 for 1h with and without 1 μM Fer-1 in fresh medium without palbociclib or doxorubicin. Trypsinized cells were collected by centrifugation at 800xg for 1min and washed with 1 mL Hank's balanced salt solution (HBSS). Cell pellet was resuspended in 500 μL HBSS containing 1 μM C11-Bodipy (D3861, ThermoFisher) and incubated for 15–20 min at 37°C. Cells were collected by centrifugation and washed once with 500 μL HBSS, resuspend in 300 μL HBSS (control cells) or 100 μL HBSS for palbociclib or doxorubicin treated cells to adjust the cell number for flow cytometry analysis. The cells were measured using ACEA Novocyte using FITC and PE channels for green and red fluorescence, respectively. Lipid peroxidation was calculated as the ratio of green and red signal. For fluorescence microscopy detection of C11-Bodipy probe, Etaluma LS620 microscope was used.

Holographic and time-lapse imaging

Holographic imaging of RLS3 treated cells were performed with Holomonitor M4 quantitative phase microscope (Phase Holographic Imaging PHI AB, Sweden). Cells were plated on 6-well plates (Sarstedt, Cat.No. 83.3920) and incubated for 3 days in the presence or absence of 50 nM doxorubicin or 1 μM palbociclib. Fresh medium without doxorubicin and Palbociclib, but containing RLS3 was added and cells were imaged every 3 min for 24 h on plates covered with HoloLids (Cat.No. 71120). Quantification of the images was performed using the Holomonitor App Suite software. For GPX4 KO cells, cells were maintained with 1 μM Fer-1 and after washing out Fer-1, cells were imaged for 6 h.

For cell cycle and nuclear size analysis, RPE1 cells expressing fluorescent cell cycle reporter mScarlet-PCNA were used.[57] A total of 3×10^3 cells were seeded on 8-Well chambered glass bottom slides (Cellvis, C8-1.5H-N) for one day before being treated with or without 200 nM Palbociclib for 48 h. The medium was replaced with complete phenol red free DMEM/F12 for imaging under a Nikon Ti2 inverted widefield fluorescence microscope equipped with a Lumencor Sola SE 365 light source and an Okolab stage incubator (OKO) maintained at 37°C with 5% CO2 and 80% humidity. The cells were observed under a 20× plan apo objective (NA 0.75) and images captured using a Photometrics Prime BSI camera with a pixel resolution of 2048 × 2048. A filter set of 560/40 nm EX, 585 nm BS, 630/75 nm EM was used. A single DIC image and the corresponding fluorescent image were taken at 5-min intervals. After 3 h, 100 nM ML162 was added, and the cells were imaged for another 7 h. These timelapse microscopy images were saved as individual multi-channel TIF files for analysis.

Nuclear segmentation, cell cycle quantification and single cell lineage analysis

The mScarlet-PCNA timelapse images were segmented using a custom pre-trained deep-learning based StarDist model.[58] The instance segmentation of the nucleus was subsequently saved as multi-channel greyscale TIF images and analyzed by SC-Track (v0.0.9) to generate single cell lineages as described.[37] The cell tracking results were analyzed using scikit-image (v0.22.0) to obtain a time series of the cell area, mScarlet-PCNA mean intensity and variance for each segmented nucleus for each respective single cell linage. The resulting single cell tracks were filtered to remove single cell instances that left the field of view during the timelapse microscopy experiment, and the variance contained in the mScarlet-PCNA intensity was used to classify cells that entered S-phase. The cell cycle tracks were summarized with R and plotted for individual cells as a bar chart. The variance (σ2) of nuclear area for each cell throughout the experiment was calculated and data binned based on initial nuclear area in 50 μm^2 intervals. Statistical difference was evaluated using Mann-Whitney test.

Imaging and flow cytometry quantification of the labile iron pool

RPE1 cells were treated with palbociclib or doxorubicin for 3 days as before or left untreated. For microscopy, 3×10^3 cells were seeded on μ-Slide 8 Well chamber slides (80806, ibidi) and treated with or without palbociclib. Prior to imaging, FerroOrange (F374, Dojindo) was diluted to 1 μM final concentration in HBSS buffer and incubated for 30 min at 37°C. Slides were placed in an Okolab stage incubator (OKO) at 37°C with 5% CO2, and 80% humidity. A Nikon Ti2 inverted fluorescence microscope equipped with a spinning-disk system (CSU-X1; Yokogawa) and operated with the MetaMorph software was used to image the cells. The cells were observed under a 60× plan apo objective (NA 1.2) and images were captured using a Photometrics Prime 95B camera. The FerroOrange stain were visualized using laser lines at the wavelengths 561 nm. A z stack of eleven 0.5 μm slices was captured to visualize the entire height of the cell. Images were processed using Fiji software (v.1.54). For flow cytometry, FerroFarRed (SiRhoNox-1, GC20134, GlpBio) was diluted in serum-free cell culture medium at 5 μM final concentration and incubated for 1 h

at 37°C. In parallel, negative control samples with FerroFarRed and 100 μM 2,2′-bipyridyl were processed. Cells were trypsinized and resuspended in PBS followed by immediate analysis using ACEA Novocyte flow cytometer. The background fluorescence from cells treated with bipyridyl was deducted from the mean far-red fluorescence signal on Qdot 655-A channel and normalized with FSC-A channel to control for cell size.

Imaging and flow cytometry quantification with ER tracker

3×10^3 RPE1 cells were seeded on μ-Slide 8 Well chamber slides (80806, ibidi) and treated with or without palbociclib for 3 days. Prior to imaging, ER Tracker Green (E34251, ThermoFisher) was diluted to 1 μM final concentration in HBSS buffer and incubated for 30 min at 37°C. The cells were imaged similarly to the FerroOrange samples, except that ER Tracker Green stain was illuminated using a 488 nm laser. For flow cytometric quantification, cells were stained for 30 min with 1 μM ER Tracker Green. For ER tracker experiments with STF-083010, cells were incubated with 50 nM doxorubicin and varying concentrations of STF-083010 for 3 days, before staining with ER Tracker and analysis using ACEA Novocyte flow cytometer.

Absolute quantification of lipids

RPE1 cells split on 15 cm dishes (5×10^5/mL) with or without 50 nM Dox (6 replicates). As a positive control, 3 dishes of RPE1 cells were cultured for 2 days and then treated with 1 μM SCD1 desaturase inhibitor CAY10566 for 24h. After 3 days, cells were typsinized and washed with PBS. Before the final centrifugation, an aliquot of cells was counted with Countstar to obtain cell count and cell size. Cell pellets were frozen in liquid nitrogen and transferred to −80°C. Absolute quantification of lipids was performed at Biotree (Shanghai, China). Briefly, for metabolite extraction the samples were homogenized in water using sonication after which extraction solution containing internal standards was added. **Lipid extraction was performed using methyl-*tert*-butyl ether (MTBE).** Lipids were separated using an SCIEX ExionLC series UHPLC System with mobile phase A consisting of 40% water, 60% acetonitrile and 10 mM ammonium formate, and the mobile phase B consisting of 10% acetonitrile and 90% isopropanol and 10 mM ammonium formate. Separated lipids were measured using AB Sciex QTrap 6500+ mass spectrometer and quantified using Biobud-v2.0.7 software. Quantitative analysis was performed based on calibration curves constructed from known amounts of individual internal lipid class standards.

Redox phospholipidomics

RPE1 cells were treated as for absolute quantification, but in 10 cm dishes and in 4 replicates for each group. To identify RSL3 induced oxidized lipid species, cells were treated with or without 0.5 μM RSL3 for 1h before cell collection. The samples were processed and extracted as described previously.[59] Briefly, extracted phospholipids were analyzed using a Dionex Ultimate 3000 HPLC system coupled with a Q-Exactive Hybrid Quadrupole-Orbitrap mass spectrometer (Thermo Fisher Scientific). Phospholipids were separated using a Waters ACQUITY BEH HILIC (100 × 2.1 mm, 1.7 μm) column at a flow rate of 0.25 mL/min at 40°C column temperature. Gradient solvents A (acetonitrile/water, 95/5, v/v) and B (acetonitrile/water, 50/50, v/v) contained 10 mM ammonium formate. The gradient elution was as follows: 0 min, 0%B; 15 min, 50%B; 15.1 min, 100%B; 18 min, 100%; B 18.1 min, 0%B; 28 min, 0%B. Capillary spray voltage, −3.0 kV; capillary temperature, 320°C; the S-lens Rf level, 60. Analysis was performed in full MS negative mode at resolution setting of 70,000 and data-dependent-MS2 mode at resolution setting of 17,500. For the MS, the scan range, m/z 114–1700; the maximum ion injection time, 100 m. For MS2, the collision energy (CE), 24 eV; the maximum ion injection time, 50 m. An isolation window of 1.0 Da was set for the MS and MS2 scans. Peaks with a signal-to-noise ratio above 3 were matched to oxidized phospholipids based on an in-house database, with m/z values matched within 5 ppm for identification. Lipids were further filtered by retention time and confirmed using MS2 analysis, following LipidMaps guidelines (https://www.lipidmaps.org). Quantitative analysis was performed based on calibration curves constructed from known amounts of reference standards and corresponding internal standards, including CL(16:0/18:2/18:2/20:4), PC(18:1/18:1), PE(18:1/18:1), PG(18:1/18:1), PI(18:1/18:1), PS(18:1/18:1), CL(14:0/14:0/14:0/14:0), PC(16:0-d31/18:1), PE(16:0-d31/18:1), PG(16:0-d31/18:1), PI(16:0-d31/18:1), PS(16:0-d31/18:1).[59,60]

RNAseq

RPE1 cells were plate in 10 cm dishes with 4 replicates for DMSO control, 50 nM Doxorubicin and Doxorubicin with ferrostatin-1 groups. 5 μM Fer-1 was added at the time of plating and additional 5 μM added after 2 days. Cells were directly lysed using 1 mL Trizol reagent. Sequencing libraries were generated at Novogene (Beijing, China) using NEBNext UltraTM RNA Library Prep Kit for Illumina. The clustering of the indexed samples was performed on a cBot Cluster Generation System using TruSeq PE Cluster Kit v3-cBot-HS (Illumina) and 150 bp paired-end reads were sequenced on Illumina Novaseq 6000. After removal of poor-quality reads and index sequences, the remaining reads were mapped against human transcriptome (Ensembl v109) using Salmon (version 1.3.0) to obtain transcript abundances. Gene level summaries were generated by *tximport* resulting in the final count table.

Double palbociclib synchronization

The confluency of the cells should be no more than 30%–40% at the time of first palbociclib arrest. 150 nM palbociclib was added to the cells for 16h followed by 3 washes with PBS and culture in fresh medium for 8 h. Palbociclib (150 nM) was added again for a

second 16 h arrest. The cells are either used as such (typically >95% G1) or released from the cell-cycle arrest using another 3 washes with PBS and collected for 8 and 12 h to obtain cells for obtaining populations enriched in S and G2/M cells, respectively.

Proteomics

RPE1 cells expressing Fucci-CA2 (TranSheep Bio, Shanghai) cells were sorted after a double-palbociclib arrest (see above). Briefly, cells were collected by trypsinization and resuspended in PBS with 1 mM EGTA. Sorting was performed using a BD Influx Cell Sorter. Preliminary sorting experiments showed that this instrument separates cells by size better using side-scatter SSC than forward scatter FSC. The cells were sorted into four populations based on the SSC scatter signal of the 488 nm laser. An aliquot of each fraction was used to measure average cell diameter and the cell cycle phase. The remaining cells were snap-frozen in liquid nitrogen and processed for proteomics at Novogene (Beijing, China). Cells were lysed in 8 M Urea, 100 mM triethylammonium bicarbonate (TEAB) buffer, pH 8.5), followed by ultrasonication. Soluble proteins were reduced with 10 mM DTT for 1 h at 56°C, alkylated with iodoacetamide and digested with trypsin. The resulting peptides were desalted with C18 column, and each sample labeled with unique TMT label before pooling and mass spectrometry. Proteomics analyses were performed using an EASY-nLCTM 1200 UHPLC coupled with a Q Exactive HF-X mass spectrometer (Thermo Fisher) in a data-dependent acquisition (DDA) mode. Peptide identification was done by searching against human proteome with the Proteome Discoverer 2.5 software (Thermo Fisher). This resulted in the identification of proteins with fragment mass tolerance of 0.02 Da and peptide/protein identification FDR<0.01, detected across all 12 samples with at least one peptide. Significantly scaling proteins were deemed as those with p value < 0.05 adjusted for multiple testing correction (Benjamini-Hochberg method).

Western blotting and immunofluorescence

Cells were incubated as detailed in the text and figure legends, washed with PBS and lysed with 1% NP40-PBS for WB. Proteins were separated on 4–12% or 4–20% SurePAGE Bis-Tris gels (Genscript) and transferred on PVDF membrane (Merck Millipore, ISEQ00010). Membranes were blocked with QuickBlock Blocking Buffer (Beyotime, P0252), incubated with primary antibodies in diluted in QuickBlock or SignalUp buffer (Beyotime, P0256 and P0272, respectively), followed by AlexaFluor Plus 680 or 800 conjugated secondary antibodies (Invitrogen, A32735 and A32729). The signals were detected with LiCOR Odyssey imager.

For immunofluorescence, cells were fixed with 4% PFA, blocked and permeabilized with 5% FBS/0.3% Triton X-100 in PBS, and stained with 1:100 dilution of Ki67 rabbit monoclonal antibody and 1:200 dilution of donkey anti-rabbit IgG. Nuclei were counterstained with DAPI (Beyotime, Cat.No. C1006) and imaged under Etaluma LS620 microscope.

QUANTIFICATION AND STATISTICAL ANALYSIS

To evaluate linear mode validity in essentiality analysis, homoscedasticity was assessed using Breusch-Pagan test using *bptest* function in *lmtest* library (v. 0.9–37). Normality of residuals was checked by Shapiro-Wilk test using *shapiro.test* function. These values were used to evaluate the goodness of fit for individual genes and thereby prioritize genes for further computational and experimental analysis. Significant test values ($p < 0.05$) in Breusch-Pagan or Shapiro-Wilk test indicate that linear model assumptions may not be valid. Note that the Shapiro-Wilk's test is influenced by sample size: With small sample sizes, non-normality may not be detected, and normality may be unjustly rejected with large sample size ($n > 100$).

To compare groups in experimental analyses, ANOVA followed by Tukey's post-hoc test with more than 3 groups and two-sided t test when comparing two groups. Statistical analyses were performed in R. Number of samples along with mean and description of error bars are reported in each figure legend. Experimental sample data were assumed to be normally distributed, but this was not specifically tested.